Generalized Lapse Rate Formulas for Use in Entraining CAPE Calculations

JOHN M. PETERS,[a] JAKE P. MULHOLLAND,[a] AND DANIEL R. CHAVAS[b]

[a] *Department of Meteorology, Naval Postgraduate School, Monterey, California*
[b] *Department of Earth, Atmospheric, and Planetary Sciences, Purdue University, West Lafayette, Indiana*

(Manuscript received 5 May 2021, in final form 7 September 2021)

ABSTRACT: Common assumptions in temperature lapse rate formulas for lifted air parcels include neglecting mixing, hydrostatic balance, the removal of all condensate once it forms (pseudoadiabatic), and/or the retention of all condensate within the parcel (adiabatic). These formulas are commonly derived from the conservation of entropy, which leads to errors when nonequilibrium mixed-phase condensate is present. To evaluate these assumptions, a new general lapse rate formula is derived from an expression for energy conservation, rather than entropy conservation. This new formula incorporates mixing of the parcel with its surroundings, relaxes the hydrostatic assumption, allows for nonequilibrium mixed-phase condensate, and can be formulated for pseudoadiabatic or adiabatic ascent. The new formula is shown to exactly conserve entropy for reversible ascent. Predictions by the new formula are compared to that of older and less general formulas. The errors in previous formulas arise from the assumption of hydrostatic balance, which results in considerable warm biases due to the neglect of the energy sink from buoyancy. Predictions of ascent with entrainment using the new formula are then compared to parcel properties along trajectories in large eddy simulations. Simulated parcel properties are better predicted by the formula using a diluted analogy to adiabatic ascent, wherein condensate is diluted at the same rate as other parcel properties, than by the diluted analogy to pseudoadiabatic ascent, wherein all condensate is removed. These results suggest that CAPE should be computed with adiabatic, rather than pseudoadiabatic, parcel ascent.

KEYWORDS: Clouds; Conservation equations; Convective storms; Convective-scale processes; Thermodynamics; Large eddy simulations

1. Introduction

A wide range of forecasting, research, and teaching applications require one to vertically displace an air parcel and compute its subsequent properties using parcel theory. Perhaps the most widely known and taught example of parcel theory is in the computation of convective available potential energy (CAPE; Moncrieff and Miller 1976), which is a useful tool for forecasting and parameterizing moist atmospheric convection. A litany of other weather forecasting parameters, which are too numerous to comprehensively list here, use parcel theory (Thompson et al. 2003, 2007). Comparatively sophisticated parcel-theory-like calculations that incorporate entrainment are often used to estimate the properties of convective updrafts in theory (Morrison 2017), cumulus parameterizations (the entraining plume model; Simpson and Wiggert 1969; Arakawa and Schubert 1974), and in computing entrainment CAPE (ECAPE; Zhang 2009; Peters et al. 2020a). Because of the ubiquity of parcel theory calculations, there are a wide range of methods and approximations involved in calculating the properties of vertically displaced air parcels, each with their own unique set of advantages and disadvantages.

One common method for computing lifted air parcel properties is via the numerical integration of temperature (Prosser and Foster 1966; Emanuel 1994; Marquet 2016) or potential temperature (Bryan and Fritsch 2004) lapse rate equations. Explicit numerical integration of lapse rate formulas offers a computational advantage over implicit vertical integration techniques (Davies-Jones 2008) because only one or two operations are needed at each level when using explicit techniques, whereas many operations are often needed for iterative variable solutions when using implicit techniques. Lapse rate formulas are also useful components of theoretical analyses (Durran and Klemp 1982) and are fundamental course material in atmospheric thermodynamics courses. For instance, a simple Internet search for "moist adiabatic lapse rate" yields lapse rate derivations in course notes from numerous universities around the world. Furthermore, the American Meteorological Society (AMS) glossary lists three different lapse rate definitions (https://glossary.ametsoc.org/wiki/Adiabatic_lapse_rate). The starting point for these derivations often involves the assumed adiabatic conservation of various definitions of moist entropy s_m or, less commonly, moist static energy. There are also a variety of assumptions regarding the behavior of precipitation, heat capacities, latent heat, and conserved variables in these lapse rate derivations. Despite the ubiquity of lapse rate equations in research and forecasting, surprisingly few attempts have been made to compare such formulas and to determine how the underlying assumptions for such formulas affect their efficacy.

Lapse rate equations typically describe the behavior of air parcels that do not experience mixing. However, it is well known that undiluted parcels are virtually absent in the middle to upper troposphere in tropical moist convective updrafts outside of tropical cyclones (Zipser 2003; Kuang and Bretherton 2006; Romps and Kuang 2010) and probably only occur in supercell thunderstorms in the midlatitudes (Peters et al. 2019, 2020a,b), which are somewhat rare compared to other modes of convection. Thus, the relevance of calculations (such as CAPE) that use undiluted adiabatic parcels has been

---

Corresponding author: J. Peters, jmpeters@nps.edu

DOI: 10.1175/JAS-D-21-0118.1

questioned by these previous authors. Despite this knowledge, the use of ECAPE in forecasting has not yet gained traction. Rather many commonly used CAPE formulations calculate pseudoadiabatic parcel ascent (Davies-Jones 2008; Blumberg et al. 2017), wherein all condensate is assumed to fall out of an air parcel immediately as it forms [see section 4.7 in Emanuel (1994)]. However, though precipitation may be envisioned as a form of "mixing," calculations generally ignore the turbulent mixing of gas and precipitation constituents between a parcel and its surroundings and therefore do not properly predict diluted parcel ascent. In fact, there has been no clear demonstration of whether pseudoadiabatic or adiabatic parcel ascent is most "relevant" to deep convection in past literature. Moreover, analyses of radiosondes in the tropics suggest that environmental temperature more closely resembles that of a parcel lifted adiabatically (Xu and Emanuel 1989) rather than pseudoadiabatically, hinting that adiabatic ascent may be more relevant to deep convection than pseudoadiabatic ascent.

Motivated by the aforementioned knowledge gaps, the objectives of this article are as follows:

1) to derive a general lapse rate formula from an expression for energy conservation that minimizes the common approximations that have been used in the past, and allows for open-system effects such as entrainment;
2) to use this formula to address the consequences of approximations used in past formulas; and
3) to use this formula to address the following hypothesis: the dissipation rate with height of condensed water in large-eddy simulations (LES) correlates with parcel dilution. Consequently, the properties of undiluted parcels in LES are better described by adiabatic than by pseudoadiabatic ascent. Thus, CAPE computed with adiabatic parcels is more relevant to the behavior of deep convection than CAPE computed with pseudoadiabatic parcels.

The organization of this paper is as follows: section 2 derives the new lapse rate formulas and compares them to formulas in previous articles and books. Section 3 compares predictions from these new lapse rate formulas to output along trajectories from LES to evaluate the accuracy of the formulas, and to address our hypothesis. Finally, section 4 provides a summary, conclusions, and discussion.

2. Derivations and analyses of lapse rate formulas

a. Profiles used for evaluating formulas

For analyzing the behavior of the formulas described in subsequent sections, we applied these formulas to two analytic vertical thermodynamic profiles using the method of Chavas and Dawson (2021, hereafter CD21); the profiles are shown in Fig. 1. These profiles are defined by a surface temperature T_{sfc}, a surface mass fraction $q_{v,\mathrm{sfc}}$, a constant moist static energy (MSE; defined later) between the surface and top-of-planetary boundary layer (PBL) height z_{PBL}, a linearly decreasing dry static energy (DSE) between z_{PBL} and the tropopause height z_{trop} with rate of change c, an isothermal stratosphere set to the T at z_{trop}, and a constant relative humidity $\mathbb{H}$ above z_{PBL}. The two profiles take the following parameter values:

1) $q_{v,\mathrm{sfc}} = 11.6$ g kg^{-1}, $T_{\mathrm{sfc}} = 295$ K, $z_{\mathrm{PBL}} = 650$ m, $\mathbb{H} = 0.85$, $z_{\mathrm{trop}} = 12\,000$ m, and $c = 0.35(c_{pd}/z_{\mathrm{trop}})$ J kg^{-1}m^{-1}, where c_{pd} is the specific heat of dry air. The CAPE for undiluted parcels lifted from the surface is ~1500 J kg^{-1}, as will be shown later. We refer to this profile as CD21 CAPE1 (Fig. 1a).
2) $q_{v,\mathrm{sfc}} = 15.7$ g kg^{-1}, $T_{\mathrm{sfc}} = 301.5$ K, $z_{\mathrm{PBL}} = 850$ m, $\mathbb{H} = 0.85$, $z_{\mathrm{trop}} = 12\,000$ m, and $c = 0.3(c_{pd}/z_{\mathrm{trop}})$ J kg^{-1}m^{-1}. The DSE also instantaneously jumped by $T_{\mathrm{jump}}c_{pd}$ J kg^{-1} at z_{PBL}, where $T_{\mathrm{jump}} = 1$ K, to create a small capping inversion and prevent widespread errant convection in the simulations analyzed later. The CAPE for undiluted parcels lifted from the surface is greater than 4000 J kg^{-1}, as will be shown later. We refer to this profile as CD21 CAPE2 (Fig. 1b).

b. Starting point for derivations

We begin our derivations with the following definition of specific enthalpy k (see appendix A) for moist air:

$$k = c_{pml}T + L_v q_v - L_i q_i, \tag{1}$$

where $c_{pml} \equiv (1 - q_t)c_{pd} + q_t c_l$, $q_t = q_v + q_l + q_i$, c variables are specific heats at constant pressure, L variables are latent heats of phase change, and q variables are *mass fractions* (see Table 1 for specific variable definitions). In atmospheric science, the first term is commonly referred to as "sensible heat" and the sum of the second and third terms as "latent heat." Hence forth, we make the "standard" Rankine–Kirchhoff (RK) approximations (Romps 2021) that the heat capacities of water vapor, liquid, and ice are constant; we assume that all condensate has the same temperature as the air it resides within; and we neglect the volume of condensate (Emanuel 1994). These approximations are necessary to make any headway in analytically deriving equations for the moist thermodynamics of the atmosphere.

Given these assumptions, we may use the chain rule to write the rate of change of k as an air parcel changes its height as

$$\frac{dk}{dz} = \frac{\partial k}{\partial T}\frac{dT}{dz} + \frac{\partial k}{\partial q_t}\frac{dq_t}{dz} + \frac{\partial k}{\partial q_v}\frac{dq_v}{dz} + \frac{\partial k}{\partial q_i}\frac{dq_i}{dz}, \tag{2}$$

where $d/dz \equiv (1/w)d/dt$. Next, we expand $d/dz = (d/dz_{\mathrm{ad}}) + (d/dz_d)$, where subscript ad is the rate of change with height exclusively due to adiabatic processes, and subscript d is that exclusively from diabatic processes. This expansion gives

$$\begin{aligned}\frac{dk}{dz} = &\underbrace{\frac{\partial k}{\partial T}\frac{dT}{dz_{\mathrm{ad}}} + \frac{\partial k}{\partial q_t}\frac{dq_t}{dz_{\mathrm{ad}}} + \frac{\partial k}{\partial q_v}\frac{dq_v}{dz_{\mathrm{ad}}} + \frac{\partial k}{\partial q_i}\frac{dq_i}{dz_{\mathrm{ad}}}}_{\dfrac{dk}{dz_{\mathrm{ad}}}}\\ &+\underbrace{\frac{\partial k}{\partial T}\frac{dT}{dz_d} + \frac{\partial k}{\partial q_t}\frac{dq_t}{dz_d} + \frac{\partial k}{\partial q_v}\frac{dq_v}{dz_d} + \frac{\partial k}{\partial q_i}\frac{dq_i}{dz_d}}_{\dfrac{dk}{dz_d}}.\end{aligned} \tag{3}$$

Diabatic processes are hereafter denoted by the symbol ϵ (e.g., $dT/dz_d = \epsilon_T$, $dk/dz_d = \epsilon_k$). We will neglect all diabatic

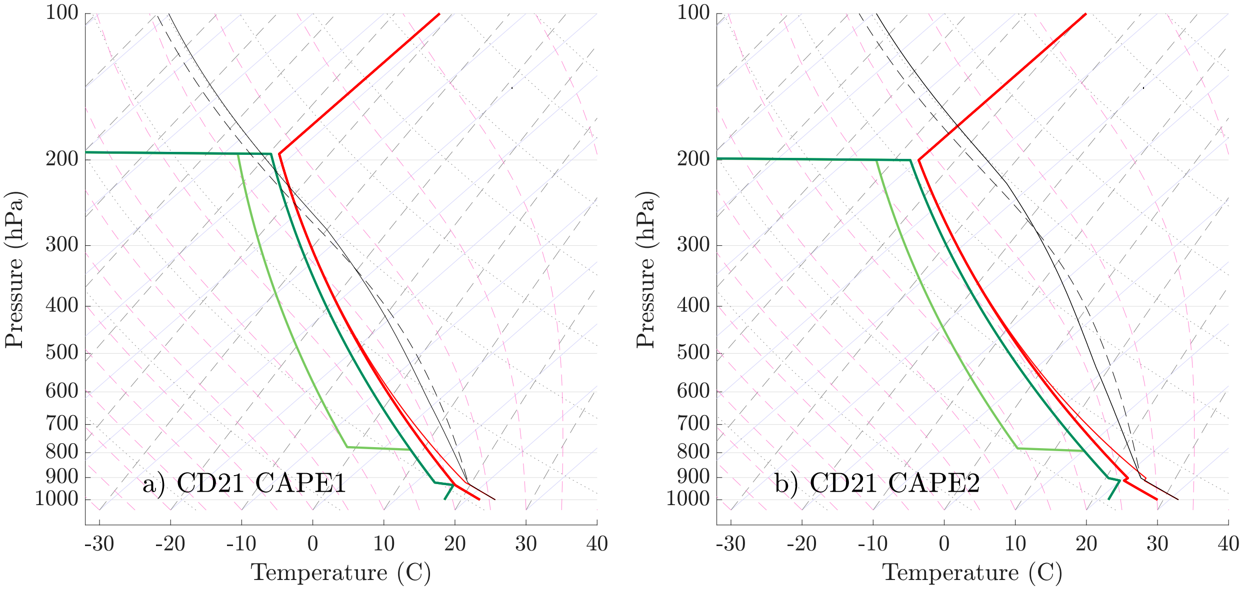

FIG. 1. Skew T–log$p$ diagrams of the CD21 (a) CAPE1 profile and (b) CAPE2 profile. The quantities shown are T (thick red line; °C), virtual temperature T_v (thin red line; °C), dewpoint temperature T_d (green lines; $\mathbb{H}2$: dark green, $\mathbb{H}1$: light green), and the density temperature T_ρ (see Table 1) of surface parcels lifted adiab irev (solid black line; °C) and pseudo (dashed black line; °C) using the formulas derived in this study.

processes (e.g., radiation, dissipative heating, surface fluxes) aside from mixing and precipitation. For an adiabatic parcel, the governing equation for k is

$$\frac{dk}{dz_{\mathrm{ad}}} = \frac{1}{\rho}\frac{dp}{dz}. \tag{4}$$

This equation is simply d/dz applied to the First Law of Thermodynamics. Combining Eqs. (3) and (4), and substituting in our ϵ terms, gives

$$\frac{dk}{dz} = \frac{1}{\rho}\frac{dp}{dz} + \underbrace{\frac{\partial k}{\partial T}\epsilon_T + \frac{\partial k}{\partial q_t}\epsilon_{q_t} + \frac{\partial k}{\partial q_v}\epsilon_{q_v} + \frac{\partial k}{\partial q_i}\epsilon_{q_i}}_{\epsilon_k}. \tag{5}$$

In conjunction with Eq. (5), we will keep track of the q_t budget, which is

$$\frac{dq_t}{dz} = \epsilon_{q_t}, \tag{6}$$

where ϵ_{q_t} represents sources/sinks of q_t due to mixing and hydrometeor exchanges. The latent heats L_v and L_i are obtained via Kirchoff's relations as

$$\frac{dL_v}{dT} = c_{pv} - c_l, \text{ and} \tag{7}$$

$$\frac{dL_i}{dT} = c_l - c_i. \tag{8}$$

Integrating these formulas using the triple point temperature T_{trip} and known reference latent heats at this temperature $L_{v,\mathrm{trip}}$ and $L_{i,\mathrm{trip}}$ as a lower bound of integration gives $L_v = L_{v,\mathrm{trip}} + (T - T_{\mathrm{trip}})(c_{pv} - c_l)$ and $L_i = L_{i,\mathrm{trip}} + (T - T_{\mathrm{trip}})(c_l - c_i)$.

Saturation vapor pressures over liquid $\mathbb{E}_{s,l}$ and ice $\mathbb{E}_{s,i}$ were determined via the Clausius–Clapeyron equation, such that

$$\frac{d\mathbb{E}_{s,l}}{dT} = \frac{L_v\mathbb{E}_{s,l}}{R_vT^2}, \text{ and} \tag{9}$$

$$\frac{d\mathbb{E}_{s,i}}{dT} = \frac{(L_v + L_i)\mathbb{E}_{s,i}}{R_vT^2}. \tag{10}$$

The terms $\mathbb{E}_{s,l}$ and $\mathbb{E}_{s,i}$ are obtained by analytically integrating Eqs. (9) and (10) from T_{trip} to T, and by setting $\mathbb{E}_{s,l} = \mathbb{E}_{s,i} = \mathbb{E}_{\mathrm{ref}}$ at T_{trip}. Note that more accurate empirical formulas, such as those obtained by Bolton (1980), were not used here to maintain self-consistency among our equations [as was done in Bryan and Fritsch (2004)]. Saturation mass fractions over liquid $q_{v,s,l}$ and ice $q_{v,s,i}$ are obtained from Eqs. (9) and (10) by noting that

$$q_{v,s,l} = (1 - q_t)\varphi\left(\frac{p}{\mathbb{E}_{s,l}} - 1\right)^{-1} \text{ and} \tag{11}$$

$$q_{v,s,i} = (1 - q_t)\varphi\left(\frac{p}{\mathbb{E}_{s,i}} - 1\right)^{-1}, \tag{12}$$

where $\varphi \equiv R_d/R_v$.

Next we write variables as the sum of a horizontally and temporally invariant hydrostatically balanced reference state, denoted by a subscript 0, and a perturbation from this reference state, denoted by a prime ($'$). This allows us to rewrite the enthalpy budget equation [Eq. (2)] in the following form

TABLE 1. List of symbol definitions. All constants are set to their values in the "constants.F" module in the CM1 source code. Formulas are provided when applicable.

Parameter	Meaning	Unit
q_v	Water vapor mass fraction (i.e., specific humidity, ratio of water vapor mass to total air mass)	kg kg^{-1}
q_l	Liquid water mass fraction	kg kg^{-1}
q_i	Ice mass fraction	kg kg^{-1}
q_t	Total water mass fraction	kg kg^{-1}
$q_{v,s}$	Saturation mass fraction	kg kg^{-1}
$q_{v,s,l}$	Saturation mass fraction with respect to liquid only	kg kg^{-1}
$q_{v,s,i}$	Saturation mass fraction with respect to ice only	kg kg^{-1}
c_{pd}	Specific heat capacity of dry air at constant pressure	J kg^{-1} K^{-1}
c_{pv}	Specific heat capacity of water vapor at constant pressure	J kg^{-1} K^{-1}
c_l	Specific heat capacity of liquid water	J kg^{-1} K^{-1}
c_i	Specific heat capacity of ice water	J kg^{-1} K^{-1}
c_{pm}	Specific heat of moist air: $(1 - q_t)c_{pd} + q_v c_{pv} + q_l c_l + q_i c_i$	J kg^{-1} K^{-1}
c_{pmv}	Specific heat of moist, unsaturated air: $(1 - q_t)c_{pd} + q_v c_{pv}$	J kg^{-1} K^{-1}
c_{pml}	Alternative specific heat of moist air: $(1 - q_t)c_{pd} + q_t c_l$	J kg^{-1} K^{-1}
R_d	Specific gas constant of dry air	J kg^{-1} K^{-1}
R_v	Specific gas constant of water vapor	J kg^{-1} K^{-1}
R_m	Specific gas constant of moist air: $(1 - q_v)R_d + q_v R_v$	J kg^{-1} K^{-1}
φ	R_d/R_v	Unitless
T_{trip}	Triple point temperature	K
T	Temperature	K
T_ρ	Density temperature: $T\left(1 - q_t + \dfrac{q_v}{\varphi}\right)$	K
$L_{v,\text{trip}}$	Reference latent heat of vaporization at T_{trip}	J kg^{-1}
$L_{i,\text{trip}}$	Reference latent heat of freezing at T_{trip}	J kg^{-1}
L_v	Latent heat of vaporization: $L_{v,\text{trip}} + (T - T_{\text{trip}})(c_{pv} - c_l)$	J kg^{-1}
L_i	Latent heat of freezing: $L_{i,\text{trip}} + (T - T_{\text{trip}})(c_l - c_i)$	J kg^{-1}
L_s	Latent heat of sublimation: $L_v + \omega L_i$	J kg^{-1}
ω	Ratio of ice to total condensate: $\dfrac{q_i}{q_l + q_i}$	Unitless
$\mathbb{E}_{s,l}$	Partial pressure of water vapor over liquid	Pa
$\mathbb{E}_{s,i}$	Partial pressure of water vapor over ice	Pa
$\mathbb{E}_{\text{ref}}$	Reference vapor pressure of 611.2 Pa	Pa
p_b	Reference pressure for potential temperature calculation of 100 000 Pa	Pa
B	Buoyancy: $g(T_\rho - T_{\rho,0})/T_{\rho,0}$	
k	Specific enthalpy: $c_{pml}T + L_v q_v - L_i q_i$	J kg^{-1}
MSE	Moist static energy: $k + gz$	J kg^{-1}
IB	Integrated buoyancy: $\displaystyle\int_{z_0}^{z} B\,dz$	J kg^{-1}
CAPE	Convective available potential energy: $\displaystyle\int_{\text{LFC}}^{\text{EL}} B\,dz$	J kg^{-1}
ϵ_ϕ	Time rate of change of an arbitrary variable ϕ due to mixing of a parcel with its surroundings: $d\phi/dt_{\text{diab}}$	Varies
ε	Fractional entrainment inverse length scale	km^{-1}
$\mathbb{H}$	Relative humidity	%
C	Passive tracer concentration	kg kg^{-1}
s_m	Specific moist entropy (Romps 2008): $c_{pm}\ln\left(\dfrac{T}{T_{\text{trip}}}\right) - R_m \ln\left(\dfrac{p}{\mathbb{E}_{\text{ref}}}\right) + R_d[1 + (\varphi + 1)q_v - q_t]\ln[1 + (\varphi + 1)q_v - q_t]$ $- R_d(1 + \varphi)q_v \ln[(1 + \varphi)q_v] - R_d(1 - q_t)\ln(1 - q_t) + q_v\left(\dfrac{L_{v,\text{trip}}}{T_{\text{trip}}}\right) - q_i\left(\dfrac{L_{i,\text{trip}}}{T_{\text{trip}}}\right)$	J kg^{-1} K^{-1}
θ_e	Equivalent potential temperature (Romps 2010): $T_{\text{trip}}\left(\dfrac{p_b}{\mathbb{E}_{\text{ref}}}\right)^{(R_d/c_{pd})} e^{(s_m/c_{pd})}$	K
θ_{ep}	Pseudoequivalent potential temperature (Bolton 1980): $T(p_b/p)^{0.2854[1 - 0.28(q_v/1 - q_v)]}\exp\left[\dfrac{q_v}{1 - q_v}\left(1 + 0.81\dfrac{q_v}{1 - q_v}\right)\left(\dfrac{3376}{T_d} - 2.54\right)\right]$	K
T_d	Dewpoint temperature for θ_{ep} calculation (Bolton 1980): $\dfrac{1}{\dfrac{1}{T - 55} - \dfrac{\ln\mathbb{H}}{2840}} + 55$	K

that is more convenient for later derivations (Peters and Chavas 2021):

$$\frac{d\mathrm{MSE}}{dz} = -B + \frac{1}{\rho}\frac{dp'}{dz} + \epsilon_k, \tag{13}$$

where

$$\mathrm{MSE} \equiv k + gz \tag{14}$$

is the moist static energy, which absorbs the component of pressure-volume work that is directly exchangeable with gravitational potential energy, and $B \equiv -g(\rho'/\rho)$ is buoyancy. Hence, the MSE of an air parcel is defined as the sum of its sensible heat, latent heat, and gravitational potential energy. Typical orders of magnitude of the individual terms are $O(d\mathrm{MSE}/dz) = 1\,\mathrm{J\,kg^{-1}\,m^{-1}}$, $O(B) = 0.1\,\mathrm{J\,kg^{-1}\,m^{-1}}$, $O[(1/\rho)dp'/dz] = 0.01$–$0.1\,\mathrm{J\,kg^{-1}\,m^{-1}}$, and $O(\epsilon_k) = 1\,\mathrm{J\,kg^{-1}\,m^{-1}}$ (Peters and Chavas 2021). Thus, all terms except for ϵ_k are typically neglected on the right-hand side of Eq. (13). However, since our goal is to obtain the most accurate possible formula, we retain the B term and only neglect the $(1/\rho)dp'/dz$ term. The omission of the p' term is motivated by both necessity and past literature. For instance, an accurate determination of p' following a vertically displaced parcel is mathematically intractable without extensive knowledge of the parcel's surroundings because the local p' is influenced by thermal and kinematic properties of the atmosphere over a large adjacent region (Davies-Jones 2002, 2003). It was further shown by Peters and Chavas (2021) that reasonably accurate predictions of parcel properties along trajectories in LES were obtainable with p' neglected. Hence, we assume that a parcel instantaneously adjusts to p_0 as it moves vertically, and $p' = 0$ in all subsequent derivations. It can be shown that when $p' = 0$, $B = g[(T_\rho - T_{\rho,0})/T_{\rho,0}]$ (see appendix B), where T_ρ and $T_{\rho,0}$ are the density temperatures of the parcel and the background environment respectively.

Thus, we may write Eq. (13) as (Riehl and Malkus 1958; Betts 1974; Romps 2015; Peters and Chavas 2021)

$$\frac{d\mathrm{MSE}}{dz} = -B + \epsilon_k, \tag{15}$$

or alternatively following Romps (2015, hereafter R15) as

$$\frac{d}{dz}(\mathrm{MSE} - \mathrm{IB}) = \epsilon_k, \tag{16}$$

where $\mathrm{IB} \equiv -\int_{z^*=z_0}^{z^*=z} B\,dz^*$ (IB is integrated buoyancy). Note that R15 considered MSE − IB to be an adiabatically conserved variable, which can be used to solve for T and q_v of an ascending parcel via an implicit numerical integration scheme that assumes this quantity remains constant. However, this type of scheme is computationally expensive, as it requires many iterations for convergence at each level moving upward. Thus, an ancillary motivation of our lapse rate derivation is to provide a new and more efficient method of solving for lifted parcel properties when MSE − IB is conserved.

Expanding the definitions of $\mathrm{MSE} = c_{pml}T + L_v q_v - L_i q_i + gz$ and $\epsilon_k = (\partial k/\partial T)\epsilon_T + (\partial k/\partial q_t)\epsilon_{q_t} + (\partial k/\partial q_v)\epsilon_{q_v} + (\partial k/\partial q_i)\epsilon_{q_i}$ in Eq. (15), evaluating the partial derivatives, rearranging, and cancelling redundant terms gives

$$c_{pm}\frac{dT}{dz} + L_v\frac{dq_v}{dz} - L_i\frac{dq_i}{dz} + g = -B + c_{pm}\epsilon_T + L_v\epsilon_{q_v} - L_i\epsilon_{q_i}, \tag{17}$$

where $c_{pm} = (1 - q_t)c_{pd} + q_v c_{pv} + q_l c_l + q_i c_i$. Note that Eq. (17) has c_{pm} (the true specific heat of the parcel) rather than c_{pml}, which is the result of cancellation of multiple terms related to dL_v/dz and dL_i/dz during the derivation.

c. *Conceptual understanding*

One major benefit of working with energy rather than entropy is the intuitive conceptual understanding that comes with energy conservation. Because MSE [Eq. (14)] is a simple linear sum of four forms of energy—sensible heat, potential energy, latent heat of vaporization, and latent heat of freezing—its decrease in temperature with height is associated *solely* with conversion between sensible heat and the other three forms. The lone exception is through the buoyancy sink, for which sensible heat is either converted to vertical kinetic energy or lost to the environment. Hence, before deriving our general lapse rate equations, we first begin with a schematic diagram of the exchanges of energy that occur within a parcel in different regimes as it rises adiabatically (Fig. 2). After the formula for each regime is derived below, a conceptual explanation is provided with reference to Fig. 2.

d. *General unsaturated lapse rate*

During unsaturated adiabatic displacements, q_v is adiabatically conserved so the only source is from diabatic exchanges of q_v with the parcel's surroundings, yielding $dq_v/dz = \epsilon_{q_v}$. We also assume that the unsaturated parcel does not contain liquid or ice, yielding $q_t = q_v$, $\epsilon_{q_t} = \epsilon_{q_v}$, and $q_l = q_i = 0$. Using these conditions, Eq. (17) reduces to

$$c_{pmv}\frac{dT}{dz} + g = -B + c_{pmv}\epsilon_T, \tag{18}$$

where $c_{pmv} \equiv (1 - q_v)c_{pd} + q_v c_{pv}$. Conceptually, the unsaturated regime is associated with a conversion of sensible heat to potential energy during ascent in the absence of mixing (Fig. 2), with an additional source or sink of energy related to the parcel's B (see section 2 in R15).

Equation (18) may be solved for the lapse rate:

$$\frac{dT}{dz} = -\frac{g}{c_{pd}}\left(\frac{1 + \dfrac{B}{g}}{\dfrac{c_{pmv}}{c_{pd}}}\right) + \epsilon_T, \tag{19}$$

where we have retained the convention from past literature to write the right-hand side (RHS) of the equation as a product of g/c_{pd} and other terms. Equation (19) is a generalization of common previous lapse rate formulas for unsaturated adiabatic parcels that neglect buoyancy and mixing effects, yielding $dT/dz = -(g/c_{pmv})$ (Durran and Klemp 1982; Emanuel 1994), and the standard "dry adiabatic lapse rate" formula that further neglects the heat capacity of q_v, yielding

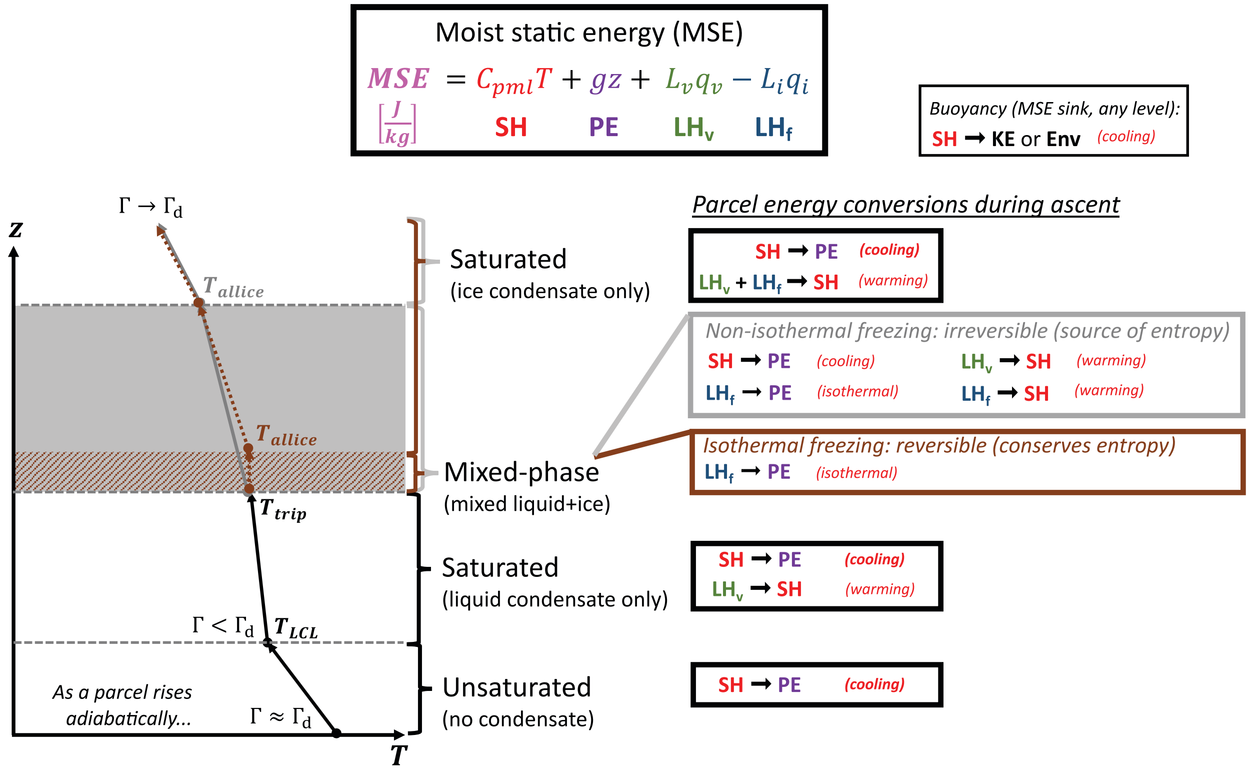

FIG. 2. Schematic diagram of the exchanges of forms of energy within a parcel as it rises adiabatically. Such energy exchanges are implicit in the lapse rate formulas presented in the text derived from conservation of moist static energy (MSE). Buoyancy is an MSE sink that converts sensible heat (SH) to vertical kinetic energy or transfers it to the environment. Note that the lapse rates (Γ) within each layer are idealized; the true saturated lapse rate varies with altitude. Γ_d is the dry adiabatic lapse rate.

$dT/dz = -g/c_{pd}$ (AMS glossary; https://glossary.ametsoc.org/wiki/Adiabatic_lapse_rate).

e. General saturated lapse rate

For a saturated parcel, we must make additional assumptions about the moisture content of the parcel to obtain a solvable equation for the lapse rate. First, we define the parameter $\omega \equiv q_i/(q_l + q_i)$. This parameter depends on both temperature and height, ranges from 0 to 1, and will discriminate liquid and ice processes. We also assume that parcels remain saturated during ascent, such that $q_v = q_{v,s}$, where the saturation mass fraction $q_{v,s}$ corresponds to the following linear combination of $q_{v,s,l}$ and $q_{v,s,i}$:

$$q_v = q_{v,s} = (1-\omega)q_{v,s,l} + \omega q_{v,s,i}. \qquad (20)$$

Combining Eq. (20) with Eq. (17), including the diabatic source terms $\epsilon_{q_{v,s}}$ and ϵ_{q_i}, and using $\epsilon_\omega = (d\omega/dT)\epsilon_T$ gives

$$\left[c_{pm} - L_i(q_t - q_{v,s})\frac{\partial\omega}{\partial T}\right]\frac{dT}{dz} + L_s\frac{dq_{v,s}}{dz} + g$$
$$= -B + \left[c_{pm} - L_i(q_t - q_{v,s})\frac{\partial\omega}{\partial T}\right]\epsilon_T + L_s\epsilon_{q_{v,s}}, \qquad (21)$$

where $L_s \equiv L_v + \omega L_i$, which represents the latent heat from condensation and sublimation during mixed-phase ascent. The $dq_{v,s}/dz$ term may be expressed in terms of dT/dt using the derivation in appendix C:

$$\frac{dq_{v,s}}{dz} = (q_{v,s,i} - q_{v,s,l})\left(\frac{\partial\omega}{\partial T}\frac{dT}{dz} + \frac{\partial\omega}{\partial z}\right) - \frac{q_{v,s}}{1-q_t}\epsilon_{q_t}$$
$$- \frac{Q_M}{p_0}\frac{dp_0}{dz} + \frac{L_M}{R_v T^2}\frac{dT}{dz}, \qquad (22)$$

where

$$Q_M \equiv \left[(1-\omega)\frac{q_{v,s,l}}{1-\mathbb{Q}_{v,s,l}} + \omega\frac{q_{v,s,i}}{1-\mathbb{Q}_{v,s,i}}\right],$$

$$L_M \equiv \left[(1-\omega)L_v\frac{q_{v,s,l}}{1-\mathbb{Q}_{v,s,l}} + \omega(L_v + L_i)\frac{q_{v,s,i}}{1-\mathbb{Q}_{v,s,i}}\right],$$

$$\mathbb{Q}_{v,s,l} \equiv \frac{q_{v,s,l}}{\varphi - \varphi q_t + q_{v,s}},$$

and

$$\mathbb{Q}_{v,s,i} \equiv \frac{q_{v,s,i}}{\varphi - \varphi q_t + q_{v,s}}.$$

We then use the fact that the reference state is, by definition, hydrostatically balanced to substitute $dp/dz = dp_0/dz = -\rho_0 g$. Previous derivations such as that of

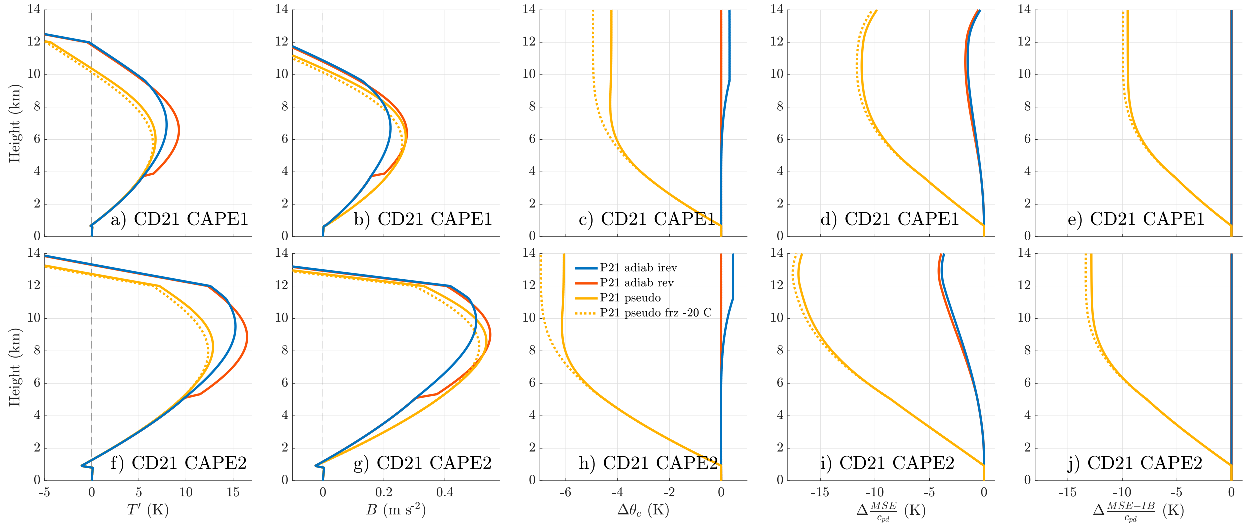

FIG. 3. Profiles of quantities along parcels lifted from the surface in the CD21 (top) CAPE1 profile and (bottom) CAPE2 profile. Quantities shown are of (a),(f) T' (K), (b),(g) B (m s^{-2}), (c),(h) $\Delta\theta_e$ (K), (d),(i) $\Delta(\mathrm{MSE}/c_{pd})$ (K), and (e),(j) $\Delta\left[(\mathrm{MSE} - \mathrm{IB})/c_{pd}\right]$ (K), where Δ denotes the difference in a quantity from its initial value. Solid blue lines indicate an adiab irev parcel with a mixed-phase region; solid red lines, an adiab rev parcel; solid yellow line, pseudo parcel with a mixed-phase region; and yellow dashed line, a pseudo parcel with ice and sublimation neglected.

Emanuel (1994) end up with a dp/dz in lieu of dp_0/dz, and these derivations subsequently assume that $dp/dz = -\rho g$. Physically, these previous derivations assume that the parcel itself remains in hydrostatic balance as it ascends, whereas our derivation has only assumed that the reference state is hydrostatically balanced, and has allowed the parcel to deviate from hydrostatic balance. The former assumption made by previous authors leads to a minor error in the resulting lapse rate formula, which is analyzed in detail later in this section.

Combining Eq. (22) with Eq. (21) gives

$$\left\{c_{pm} - \left[L_i(q_t - q_{v,s}) - L_s(q_{v,s,i} - q_{v,s,l})\right]\frac{\partial\omega}{\partial T} + \frac{L_s L_M}{R_v T^2}\right\}\frac{dT}{dz} + L_s(q_{v,s,i} - q_{v,s,l})\frac{\partial\omega}{\partial z} + \frac{L_s Q_M g}{R_{m,0} T_0} + g$$
$$= -B + \left[c_{pm} - L_i(q_t - q_{v,s})\frac{\partial\omega}{\partial T}\right]\epsilon_T + L_s\left(\epsilon_{q_v} + \frac{q_{v,s}}{1 - q_t}\epsilon_{q_t}\right), \tag{23}$$

and solving for dT/dz gives our final, general saturated lapse rate equation for an ascending parcel:

$$\frac{dT}{dz} = -\frac{g}{c_{pd}}\frac{\frac{B}{g} + 1 + \frac{L_s Q_M}{R_{m,0} T_0} - \frac{\left[c_{pm} + L_i(q_t - q_{v,s})\frac{\partial\omega}{\partial T}\right]}{g}\epsilon_T - \frac{L_s}{g}\left[\epsilon_{q_v} + \frac{q_{v,s}}{1 - q_t}\epsilon_{q_t} - (q_{v,s,i} - q_{v,s,l})\frac{\partial\omega}{\partial z}\right]}{\frac{c_{pm}}{c_{pd}} - \frac{L_i(q_t - q_{v,s}) - L_s(q_{v,s,i} - q_{v,s,l})}{c_{pd}}\frac{\partial\omega}{\partial T} + \frac{L_s L_M}{c_{pd} R_v T^2}}. \tag{24}$$

This equation must be vertically integrated in conjunction with Eq. (6) since it depends on q_t. The assumption of 100% saturation will likely cause minor errors because supersaturation is common in deep convective cores. However, this assumption is invoked in every previous lapse rate derivation that we are aware of, and Eq. (24) may therefore be considered a more accurate generalization of previous formulas, which always neglect p', assume 100% saturation, and do not account for mixed-phase condensate.

f. Adiabatic lapse rates

Before we develop explicit representations of entrainment and precipitation, we explore the behavior of our formula for nonmixing parcels. To numerically evaluate these formulas, we use the following computational logic: at a given height where T, q_t, and q_v are known, we first check to see if the parcel is saturated. If the parcel is unsaturated, we obtain T, q_t, and q_v ($q_t = q_v$) at the next level using the appropriate lapse rate equations. If the parcel is saturated, we first obtained T and q_t at the next level using the appropriate lapse rate equations. We then obtain q_v by assuming saturation, and by using the new T and p_0. The lifted condensation level is determined accurately via vertical interpolation between grid points. All numerical integrations use a vertical grid spacing of 10 m and an explicit Euler integration scheme unless stated otherwise.

We start with the case of an adiabatic parcel (i.e., $\epsilon_{q_t} = \epsilon_{q_v} = \epsilon_T = 0$) that experiences a layer of mixed-phase condensate in which liquid and ice are present at temperatures below T_{trip}. In this situation, Eq. (24) becomes

$$\frac{dT}{dz}_{\text{adiab,irev}} = -\frac{g}{c_{pd}} \times \frac{\frac{B}{g} + 1 + \frac{L_s Q_M}{R_{m,0} T_0}}{\frac{c_{pm}}{c_{pd}} - \frac{L_i(q_t - q_{v,s}) - L_s(q_{v,s,i} - q_{v,s,l})}{c_{pd}} \frac{\partial \omega}{\partial T} + \frac{L_s L_M}{c_{pd} R_v T^2}}. \tag{25}$$

To allow for a temperature range where both liquid and ice are present, we formulate ω in a manner consistent with previous studies (Khairoutdinov and Randall 2003; Bryan and Fritsch 2004; R15), where $\omega = 0$ for $T > T_{\text{trip}}$, $\omega = (T - T_{\text{trip}})/(T_{\text{cutoff}} - T_{\text{trip}})$ for $T_{\text{trip}} \le T \le T_{\text{cutoff}}$, and $\omega = 1$ for $T < T_{\text{cutoff}}$, where choices for T_{cutoff} are discussed later. As will be detailed later in this subsection, this formulation for ω results in departure from thermodynamic equilibrium in the mixed-phase region because there are a range of temperatures wherein $q_{v,s,l} \neq q_{v,s,i}$, and hence the parcel's ascent is irreversible. We therefore refer to predictions using this formula as "adiab irev."

Profiles of T' (Figs. 3a,f) and B (Figs. 3b,g) are shown for the adiab irev profiles (blue lines). Below the freezing level, these profiles are reversible and should accordingly conserve s_m and equivalent potential temperature θ_e (defined in Table 1), which is indeed the case (Figs. 3c,h). During the mixed-phase period of ascent, there is an entropy source because of the departure from thermodynamic equilibrium which is reflected by a slight increase in θ_e with height (Figs. 3c,h). Once all liquid has frozen, the parcel's ascent is once again reversible, which is reflected by a constant θ_e with height above the mixed-phase region. All of these behaviors are consistent with how an adiabatic parcel should behave. The parcel does not conserve MSE (Figs. 3d,i) because the parcel has nonzero B as it rises [Eq. (15)]; hence it *does* conserve MSE − IB, which is a requirement for an adiabatic parcel with $p' = 0$ [Eq. (16); also see R15]. Note that ω has been left general, so Eq. (25) is not uniquely valid for the mixed-phase conditions that are examined in Fig. 3. Rather, Eq. (25) is *exact* for an adiabatic parcel under the standard parcel theory assumptions for any arbitrary choice of ω, so long as ω depends only on z and T.

Next, we examine the behavior of a parcel that undergoes adiabatic reversible (hereafter "adiab rev") ascent, in which all condensate is ice at temperatures below T_{trip} and liquid at temperatures above T_{trip}. In this situation, the parcel must undergo a period of isothermal ascent when it reaches T_{trip}, at the end of which all liquid water has frozen into ice and water vapor remains in thermodynamic equilibrium over both liquid and ice (because $\mathbb{E}_{s,l} \equiv \mathbb{E}_{s,i}$ at $T = T_{\text{trip}}$). Hence, ω is effectively a function of z only, as it varies only within the isothermal layer. To quantify this isothermal layer, we rewrite Eq. (17) for an adiabatic parcel with $dT/dz = 0$ as

$$L_{v,\text{trip}} \frac{dq_{v,s}}{dz} - L_{i,\text{trip}} \frac{dq_i}{dz} + g = -B, \tag{26}$$

where $L_v = L_{v,\text{trip}}$ and $L_i = L_{i,\text{trip}}$ at $T = T_{\text{trip}}$. Dividing by the total condensate $q_c \equiv q_t - q_{v,s}$, applying the quotient rule, using Eq. (22) with $dT/dz = 0$, and making use of the fact that $\omega = q_i/q_c$ gives

$$\frac{d\omega}{dz} = \frac{B + g + (L_{v,\text{trip}} + \omega L_{i,\text{trip}}) q_{v,s} \left[1 + \frac{q_{v,s}}{\varphi(1 - q_t)}\right] \frac{g}{R_{m,0} T_0}}{L_{i,\text{trip}}(q_t - q_{v,s})} \tag{27}$$

Equation (27) is integrated upward from $\omega = 0$ at the first instance of $T = T_{\text{trip}}$ to the height where $\omega = 1$ (i.e., when all liquid has frozen). The depth of the isothermal layer is therefore set by the distance of ascent required to bring ω from 0 to 1 [i.e., integrating Eq. (27) in z].

Outside of this layer, ω is set to 0 when $T > T_{\text{trip}}$ and 1 when $T < T_{\text{trip}}$. Thus, we may set $\partial\omega/\partial T = 0$ in Eq. (25), which simplifies to

$$\frac{dT}{dz}_{\text{adiab,rev}} = -\frac{g}{c_{pd}} \frac{\frac{B}{g} + 1 + \left[1 + \frac{q_{v,s}}{\varphi(1 - q_t)}\right] \frac{q_{v,s} L_s}{R_{m,0} T_0}}{\frac{c_{pm}}{c_{pd}} + \left[1 + \frac{q_{v,s}}{\varphi(1 - q_t)}\right] \frac{L_s^2 q_{v,s}}{c_{pd} R_v T^2}}. \tag{28}$$

The adiab rev profiles (red lines in Fig. 3) undergo a brief rapid increase in T' (Figs. 3a,f) and B (Figs. 3b,g) at the freezing level because of the rapid isothermal freezing of liquid. This feature was not present in the adiab irev profile, because of the more gradual freezing with height that occurred in that profile. Accordingly, larger B occurs with the adiab rev parcel above the freezing level, up to a point just below the equilibrium level (EL) wherein the adiab irev parcel becomes slightly more buoyant (Figs. 3b,g). Since Eq. (28) describes a reversible process, the parcel should conserve entropy and indeed we find a constant θ_e throughout the parcel's path of ascent (Figs. 3c,h). The parcel should also conserve MSE − IB, and indeed we find this to be the case in Figs. 3e,j.

The physical interpretation of the differences in the behavior of the adiab irev and adiab rev parcel are understood through the MSE conservation equation [Eq. (15)] and illustrated conceptually in Fig. 2. Below the freezing level, there is a loss of sensible heat to potential energy and a small amount to the buoyancy sink that is only partially offset by the conversion of latent heat to sensible heat from phase changes. Hence the saturated lapse rate is smaller than the unsaturated lapse rate. Both the adiab irev and adiab rev parcels are reversible *below the freezing level*, and hence their properties are equivalent during this part of the ascent.

Once the adiab rev parcel reaches the isothermal layer, the energy budget simplifies for this parcel. The release of latent heat of freezing warms the parcel at exactly the rate that it is cooled doing work in adiabatic expansion as it rises, and therefore the latent heat of freezing is almost entirely converted into gravitational potential energy, with a small amount lost to either kinetic energy or the environment through the B term (Fig. 2, brown arrow). This process can be identically reversed for a parcel that descends through the isothermal mixed-phase region, and hence the term "reversible" is a sensible descriptor for this parcel. Entropy is necessarily conserved during this process (Figs. 3c,h) to ensure that the Second Law of Thermodynamics is not violated. For instance, a sink of entropy with time cannot occur for an adiabatic parcel because adiabatic implies "closed system," and $ds_m/dt \geq 0$ for a closed system. If there were a source of entropy during ascent through the mixed-phase layer, the parcel could not identically reverse the process during descent without experiencing a sink in entropy with time, and thereby violating the Second Law of Thermodynamics.

Meanwhile, adiab irev mixed-phase ascent is much more complex, combining conversions among all four forms of energy simultaneously as the parcel cools, condenses out water vapor, and freezes liquid water gradually over a deeper layer (Fig. 2, gray shaded region). Unlike the adiab rev parcel, the adiab irev parcel *does* experience a source of entropy as it ascends through the mixed-phase layer (e.g., Figs. 3c,h). Thus, the parcel cannot identically reverse the phase change if it were to descend through the region without experiencing a sink of entropy, and violating the Second Law of Thermodynamics. For instance, the parcel cannot undergo analogous mixed-phase nonisothermal melting as it descends over the same temperature range that it experienced freezing during ascent, because this would require ice to melt within the parcel while it is cooler than the melting point of ice. Hence, the parcel circuit exhibits hysteresis and thus "irreversible" is a sensible descriptor.

g. *Pseudoadiabatic lapse rate*

Finally, we examine pseudoadiabatic ("pseudo" for brevity) conditions wherein $q_t = q_{v,s}$, $q_l = q_i = 0$, $\epsilon_T = \epsilon_{q_v} = 0$, and $\epsilon_{q_t} = dq_{v,s}/dz$. Applying these assumptions to Eq. (24) gives

$$\frac{dT}{dz}_{\text{pseudo}} = -\frac{g}{c_{pd}}$$

$$\times \frac{\dfrac{B}{g} + 1 + (1 - q_{v,s})\dfrac{L_s Q_M}{R_{m,0} T_0}}{\dfrac{c_{pmv}}{c_{pd}} + \dfrac{L_s(q_{v,s,i} - q_{v,s,l})(1 - q_{v,s})}{c_{pd}}\dfrac{\partial \omega}{\partial T} + (1 - q_{v,s})\dfrac{L_M L_s}{c_{pd} R_v T^2}}. \tag{29}$$

The pseudo profile, with the temperature-dependent ω formulation used in the adiab irev formula, displays a smaller positive T' throughout much of the middle-to-upper troposphere relative to the adiab irev and rev profiles (yellow lines in Figs. 3a,f). This reduction in T' relative to the adiab irev and rev example occurs because of the large reduction in the amount of liquid that reaches the freezing level and the associated reduced latent heat of freezing added to the pseudo parcel. Despite having a smaller T', the lack of condensate loading results in the pseudo parcel having a substantially larger T_ρ (dashed black lines in Fig. 1) and B (Figs. 3b,g) than the adiab irev profile, and a comparable B to the adiab rev profile, between roughly 5 and 8.5 km [similar results were shown on p. 133 of Emanuel (1994)]. The pseudo parcel loses entropy (Figs. 3c,h), MSE (Figs. 3d,i), and MSE − IB (Figs. 3e,j) precipitously (pun intended) with height due to precipitation fallout. This entropy loss does not violate the Second Law of Thermodynamics, because a pseudo parcel is not a closed system.

Re-evaluating our equation without sublimation (i.e., $\omega = 0$, $L_s = L_v$, yellow dashed lines in Fig. 3) shows little effect on the pseudo T' and B profiles (Figs. 3a,b,f,g), because the primary source of latent heat of freezing in adiab parcels occurs from the freezing of already condensed liquid, rather than sublimation of water vapor, when $T \leq T_{\text{trip}}$, and because we do not allow for condensed liquid to remain with the pseudo parcel.

h. *Lapse rates with respect to pressure*

An alternative route to escaping the "hydrostatic dilemma" described in the previous subsection is to derive a lapse rate in terms of pressure (Bohren and Albrecht 1998; Bakhshaii and Stull 2013), rather than height. We start directly from the adiabatic First Law of Thermodynamics, which may be written as

$$\frac{dk}{dp} = \frac{1}{\rho}. \tag{30}$$

In an analogous manner to the derivation in section 2d, we rewrite this equation as

$$\left[c_{pm} - L_i(q_t - q_{v,s})\frac{\partial \omega}{\partial T}\right]\frac{dT}{dp} + L_s\frac{dq_v}{dp} = \frac{1}{\rho}. \tag{31}$$

Using a similar derivation to that in section 2d and appendix C, we write

$$\frac{dq_{v,s}}{dp} = (q_{v,s,i} - q_{v,s,l})\frac{\partial \omega}{\partial t}\frac{\partial T}{\partial p} - \frac{q_{v,s}}{1 - q_t}\frac{dq_t}{dp} - \frac{Q_M}{p} + \frac{L_M}{R_v T^2}\frac{dT}{dp}$$

Using this expression with the ideal gas law, Eq. (31) becomes

$$\frac{dT}{dp}_{\text{adiab,irev}} = \frac{1}{\rho c_{pd}} \frac{1 + \dfrac{L_s Q_M}{T_\rho R_d}}{\dfrac{c_{pm}}{c_{pd}} + \dfrac{L_s(q_{v,s,i} - q_{v,s,l}) - L_i(q_t - q_{v,s})}{c_{pd}}\dfrac{\partial \omega}{\partial T} + \dfrac{L_s L_M}{c_{pd} R_v T^2}} \tag{32}$$

where the RHS is again phrased as a modification to the pressure-dependent dry adiabatic lapse rate, $1/(\rho c_{pd})$. We have not made any hydrostatic assumption in this derivation, and at face value we have also escaped the need to neglect p' since there is no need to separate perturbation and mean state pressure in the first place. However, to vertically integrate this equation we must use set pressure levels, and since p' is not known, these levels must correspond to

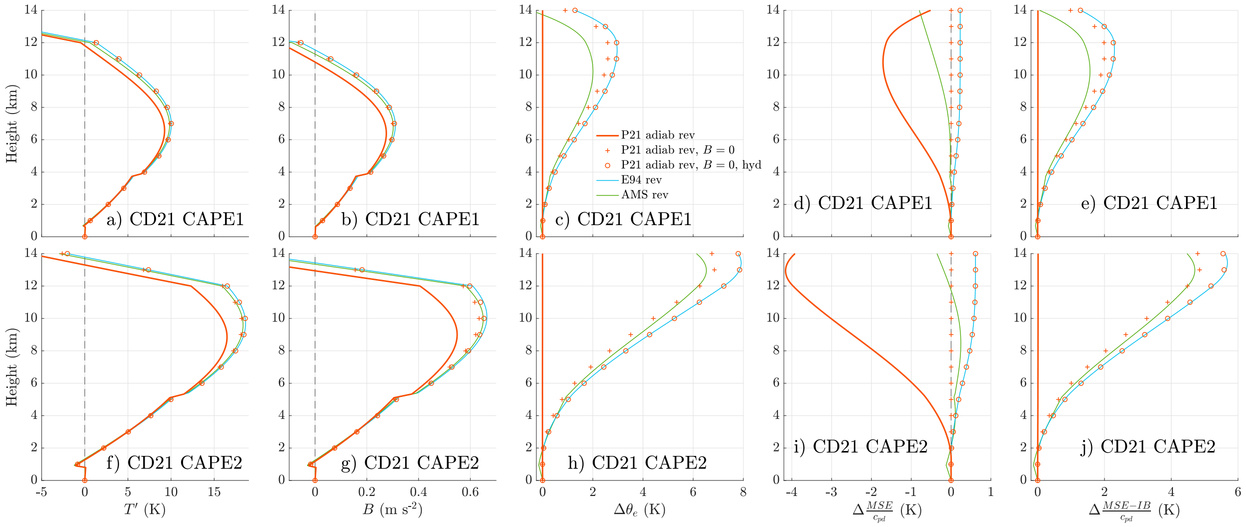

FIG. 4. Same layout as Fig. 3, but showing adiab rev ascent using the formula derived here (hereafter the "P21" formula, solid red line), using the P21 formula with $B = 0$ (red pluses), using the P21 formula with the parcel assumed to be hydrostatically balanced and $B = 0$ (red open circles), the formula from E94 (blue line), and the AMS formula listed under "moist-adiabatic lapse rate" (green line).

p_0. Thus, Eq. (32) produces an exactly equivalent profile to Eq. (25) (not shown), and appropriately conserves entropy and MSE − IB under the assumption that p' vanishes.

We obtain the analogous reversible lapse rate with respect to pressure by holding q_t constant and following the derivation of Eq. (27), but solving for $d\omega/dp$ instead of $d\omega/dz$, we obtain

$$\frac{d\omega}{dp} = -\frac{1}{p}\frac{T_\rho R_d + (L_{v,\mathrm{trip}} + L_{i,\mathrm{trip}}\omega)q_{v,s}\left[1 + \dfrac{q_{v,s}}{\varphi(1-q_t)}\right]}{L_{i,\mathrm{trip}}(q_t - q_{v,s})} \tag{33}$$

Next, by setting $\omega = 0$ for $T < T_{\mathrm{trip}}$ and $\omega = 1$ for $T > T_{\mathrm{trip}}$, Eq. (32) becomes

$$\frac{dT}{dp}_{\mathrm{adiab,rev}} = \frac{1}{\rho c_{pd}}\frac{1 + \dfrac{q_{v,s}L_s}{TR_d}}{\dfrac{c_{pm}}{c_{pd}} + \dfrac{q_{v,s}L_s^2}{c_{pd}R_v T^2}\left[1 + \dfrac{q_{v,s}}{\varphi(1-q_t)}\right]} \tag{34}$$

Finally, we obtain a pseudoadiabatic lapse rate with respect to pressure by setting $q_t = q_{v,s}$, $q_l = q_i = 0$, $\epsilon_T = \epsilon_{q_v} = 0$, and $\epsilon_{q_t} = dq_{v,s}/dp$:

$$\frac{dT}{dp}_{\mathrm{pseudo}} = \frac{1}{\rho c_{pd}}\frac{1 + (1-q_{v,s})\dfrac{L_s Q_M}{T_\rho R_d}}{\frac{c_{pm}}{c_{pd}} + (1-q_{v,s})\dfrac{L_s(q_{v,s,i} - q_{v,s,l})}{c_{pd}}\dfrac{\partial\omega}{\partial T} + (1-q_{v,s})\dfrac{L_s L_M}{c_{pd}R_v T^2}} \tag{35}$$

i. Comparison with previous reversible and pseudoadiabatic formulas

Our adiab rev and pseudo formulas, which are exact for standard parcel theory assumptions, provide a means for evaluating errors in past formulas. The most commonly referenced adiab rev formula in past literature is derived in section 4.7 [Eq. (4.7.3) therein] of Emanuel (1994, hereafter E94) from the equation for s_m [Eq. (4.5.9) therein]. An identical formula is listed in the AMS glossary under "reversible moist-adiabatic process" (https://glossary.ametsoc.org/wiki/Reversible_moist-adiabatic_process). This formula differs from ours in Eq. (28) in the absence of B and inclusion of T_ρ in the denominator here. A comparison of profiles produced by the E94 formula with our own reveals comparatively larger T' and B in the E94 formula (Figs. 4a,b,f,g). Consequently, the E94 formula does not conserve entropy or MSE − IB like ours does, and the parcel behavior it describes is not strictly reversible (Figs. 4c,e,h,j). In fact, the E94 formula more closely conserves MSE than entropy, although there is still a small source of MSE during the entire saturated portion of the parcel's ascent (Figs. 4d,i).

What is responsible for the entropy and MSE sources in the E94 formula? As was discussed earlier, in deriving his equation, E94 assumed that the *parcel* is hydrostatically balanced, whereas we have only assumed the *background state* is hydrostatically balanced. This difference is demonstrated by some simple manipulation of our equation. The two terms in our Eq. (28) that relate to this assumption are the B/g and $L_s/(R_{m,0}T_0)$ terms in the numerator. Setting $B = 0$ in our formula (red pluses in Fig. 4) gives profiles of T' (Figs. 4a,f) and B (Figs. 4b,g) that more closely match that of E94, and results in a parcel that strictly conserves its MSE (Figs. 4d,i), but not entropy (Figs. 4c,h) or MSE − IB (Figs. 4e,j). Completing the hydrostatic assumption in our formula by further replacing $L_s/(R_{m,0}T_0)$ with $L_s/(R_d T_\rho)$ results in our formula giving a curve that exactly matches the curve from E94 (red open circles in Figs. 4a–j). Another formula, which is listed under "moist-adiabatic lapse rate" in

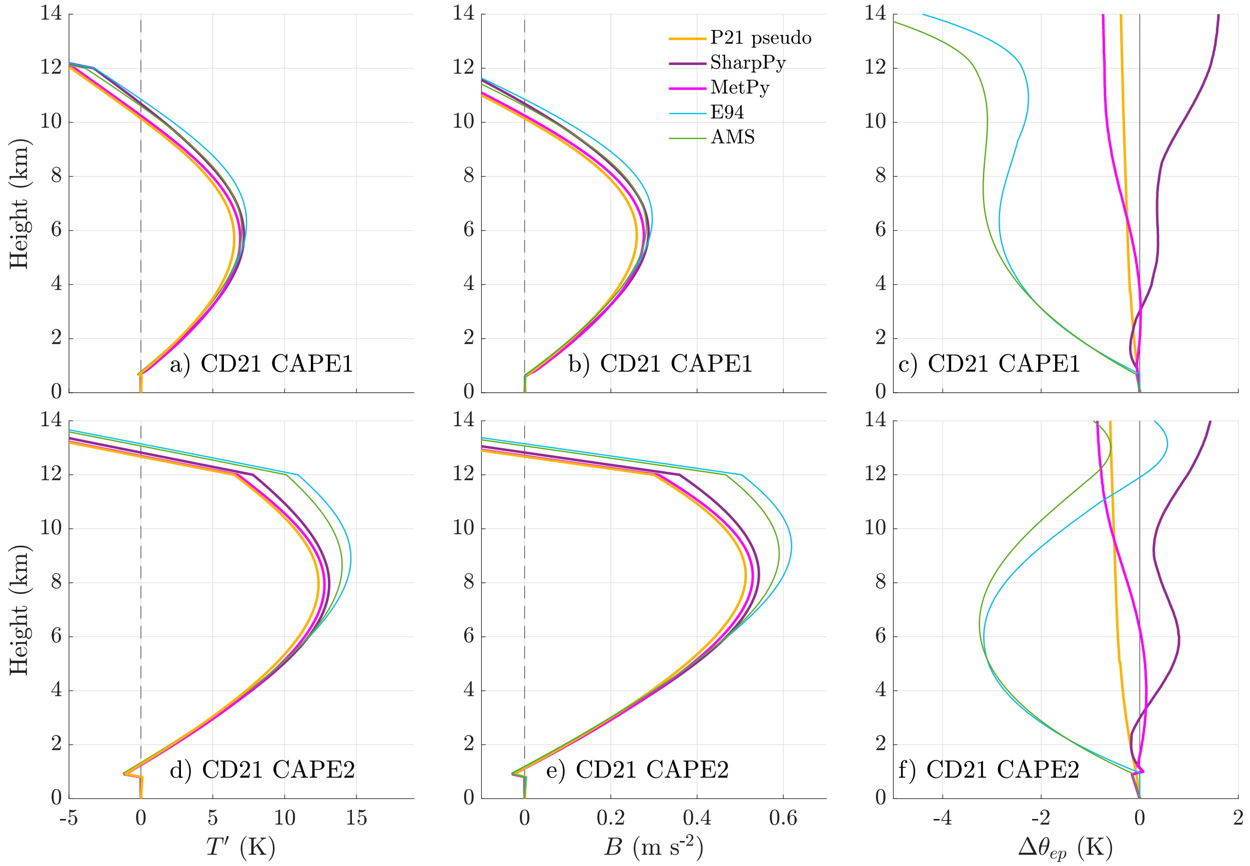

FIG. 5. (a),(d) Pseudo T' (K) predicted by the P21 pseudo formula (yellow line), SHARPpy (purple line), MetPy (magenta line), the E94 formula (cyan line), and the AMS formula (green line). (b),(e) As in (a) and (d), but showing B (m s^{-2}). (c),(f) As in (a) and (d), but showing $\Delta\theta_{ep}$ (K). Results are shown for the CD21 (top) CAPE1 profile and (bottom) CAPE2 profile.

the AMS glossary (https://glossary.ametsoc.org/wiki/Adiabatic_lapse_rate), is an approximation to the E94 formula, which assumes $c_{pmr} \approx c_{pd}$ and neglects the temperature dependence of L_s. This formula yields curves that are quite similar to that of E94, with an overprediction of T' (Figs. 4a,f) and B (Figs. 4b,g) aloft (relative to the formula derived here), and similarly experiences gradual sources of entropy (Figs. 4c,h), MSE (Figs. 4d,i), and MSE − IB (Figs. 4e,j) as it rises.

No pseudo formula is explicitly listed in E94, but one may easily be inferred by neglecting condensate in his formula, yielding an equation equivalent to that listed under "pseudoadiabatic lapse rate" in the AMS glossary (https://glossary.ametsoc.org/wiki/Pseudoadiabatic_lapse_rate; referred to here as "E94 pseudo"). Two additional profiles are included in the pseudo comparison: that of SHARPpy/NSHARP (Blumberg et al. 2017), which assumes that pseudoequivalent potential temperature θ_{ep} is conserved and iteratively solves for T and moisture at every level [as is described in Davies-Jones (2008)], and MetPy (Unidata 2021), which vertically integrates an approximation of Eq. (31) to obtain profiles of T and q_v. Since pseudo processes clearly do not conserve entropy, MSE, or MSE − IB, we do not include these quantities in our comparison. However, Bolton (1980) gives an accurate empirical formula for θ_{ep} [see his Eq. (39)]. Although this quantity is referred to by the same name as our earlier defined θ_e, a parcel with constant θ_{ep} does not conserve entropy.

Comparisons of pseudo profiles from our Eq. (29) to that of SHARPpy/NSHARP, MetPy, E94, and the AMS formulas reveal close correspondence between SHARPpy/NSHARP, MetPy, and our equation in predictions of T' (Figs. 5a,d) and B (Figs. 5b,e), and overpredictions of these quantities by the E94 and AMS formulas relative to the formula derived here. Despite the close correspondence between our formula and SHARPpy/NSHARP and MetPy, our formula more accurately conserves θ_{ep} (Figs. 5c,f) than the others due to the comparatively approximate lapse rate formula used in MetPy, and the approximations used in the iterative solution for T in SHARPpy/NSHARP [for additional details, see Davies-Jones (2008)].

j. Mixing and precipitation

The diabatic terms ϵ_T, ϵ_{q_v}, and ϵ_{q_t} are unknowns at this point, but may be represented in simple terms using the common "bulk plume" entrainment approximation (Squires and Turner 1962), wherein a cloudy parcel is assumed to mix with the properties of the far-field environment at a rate dictated by the fractional entrainment inverse length scale ε. For simplicity, we assume constant ε with height in subsequent analysis, which is justified by approximately exponential dilution rates with height along simulated parcels (not shown). Using ε, we may define our diabatic terms as

$$\epsilon_T = -\varepsilon(T - T_0), \tag{36}$$

$$\epsilon_{q_v} = -\varepsilon(q_v - q_{v,0}), \text{ and} \tag{37}$$

$$\epsilon_{q_t} = -\varepsilon(q_v - q_{v,0}) - (\varepsilon_c + \mathbb{P})(q_t - q_{v,s}), \tag{38}$$

where ε_c is the lateral mixing rate of condensates and $\mathbb{P}$ is the precipitation rate. Note that because condensates have different vertical speeds than the gas within an air parcel, they do not necessarily experience the same lateral mixing rate as gas properties, and ε is not necessarily equal to ε_c. If the hypothesis stated in section 1 were supported, we would find that combined lateral mixing and precipitation rate of condensate scales with the mixing rate of gas properties in the simulations. Hence, we set $\varepsilon_c + \mathbb{P} = \varepsilon$ in the adiab irev and adiab rev formulas, and compare the resulting predictions to the simulated trajectories. Note that in the pseudo formula, $q_t - q_{v,s} = 0$ and hence the condensate term vanishes from the equation.

These expressions were incorporated into Eqs. (24) and (6) to parameterize mixing. Note that diluted parcels cannot be strictly adiabatic or pseudoadiabatic, and cannot be lifted reversibly. However, we retain the terms adiab irev, adiab rev, and pseudo when describing forthcoming analyses of diluted parcels as a reference to the separate microphysical theories used to derive each formula.

Prior to analyzing the behavior of this formula, we perform a sanity check with the CD21 CAPE1 and CAPE2 profiles by comparing our lapse rate predictions of MSE to analytic MSE profiles, which should give reasonably similar curves. In the bulk plume approximation for entrainment, an arbitrary adiabatically conserved variable ψ obeys the equation

$$\frac{d\psi}{dz} = -\varepsilon(\psi - \psi_0), \tag{39}$$

which has the following analytic solution:

$$\psi(z) = e^{-\varepsilon z}\left[\psi_b + \int_{z^*=z_b}^{z^*=z} e^{\varepsilon z^*}\varepsilon\psi_0 dz^*\right], \tag{40}$$

where ψ_b is the value of ψ at z_b. To complete the sanity check, we first replace ψ with MSE in Eq. (40) (this equation cannot be solved with MSE − IB), and produce curves that correspond to various values of ε. We then zero out the B term in our adiab irev formula so that parcels conserve MSE rather than MSE − IB, integrate the resulting lapse rate equation, compute MSE from the result, and then compare the result to the analytic solution from Eq. (40). Curves of analytic and lapse-rate-predicted MSE closely match for all of the ε values considered (Figs. 6a,c), meaning that our lapse rate formulas "pass" the sanity check.

Finally, we briefly analyze the behavior of our formulas as a function of ε. As expected, the undiluted MSE curve from our formula with B set to 0 remains at a constant value (Figs. 6a,c), and the MSE for more diluted curves becomes progressively closer to that of MSE$_0$ (the background value; Figs. 6a,c). An analogous pattern is present for B, with large B for adiab parcels with small dilution and comparatively small (or even negative) B for parcels with large dilution (Figs. 6b,d). For large ε^{-1}, and like in the case of our analysis of Figs. 3b,g, pseudo curves generally have larger B in the middle troposphere than adiab curves, but this pattern reverses aloft near the tropopause (Figs. 6b,d). However, for smaller ε^{-1}, pseudo B becomes generally larger than adiab B throughout the depth of the region of positive B.

3. Evaluation of formulas with numerical simulations

Our general lapse rate formula [Eq. (24)] and its three approximations described above—adiabatic irreversible [Eq. (25)], adiabatic reversible [Eq. (28)], and pseudoadiabatic [Eq. (29)]—are meant to provide a simplistic representation of the behavior of parcels in real atmospheric deep convection. We therefore evaluate these assumptions against trajectories in high-resolution simulations of deep convection. Because real ascending parcels are rarely undilute, we now retain the diabatic terms in Eq. (24) via the simple parameterization for entrainment mixing given by Eqs. (36)–(38). We also use this comparison to evaluate the hypothesis from section 1, which states that the behavior of air parcels in real atmospheric ascent is more analogous to adiabatic parcel ascent than pseudoadiabatic parcel ascent.

Hence, three types are diluted parcel ascent are considered in this comparison:

1) A diluted analogy to adiab irev ascent using Eq. (24) to obtain T and Eq. (38) to obtain q_t. The formulation for ω follows that of section 2e
2) A diluted analogy to adiab rev ascent. In this scenario, Eq. (24) becomes

---

$$\frac{dT}{dz}_{\text{rev,dil}} = -\frac{g}{c_{pd}} \times \frac{\frac{B}{g} + 1 + \left[1 + \frac{q_v}{\varphi(1-q_t)}\right]\frac{L_s q_{v,s}}{R_{m,0}T_0} - \frac{c_{pm}}{g}\epsilon_T - \frac{L_s}{g}\left[\epsilon_{q_v} + \frac{q_{v,s}}{1-q_t}\epsilon_{q_t}\right]}{\frac{c_{pm}}{c_{pd}} + \left[1 + \frac{q_v}{\varphi(1-q_t)}\right]\frac{L_s^2 q_{v,s}}{c_{pd}R_v T^2}}, \tag{41}$$

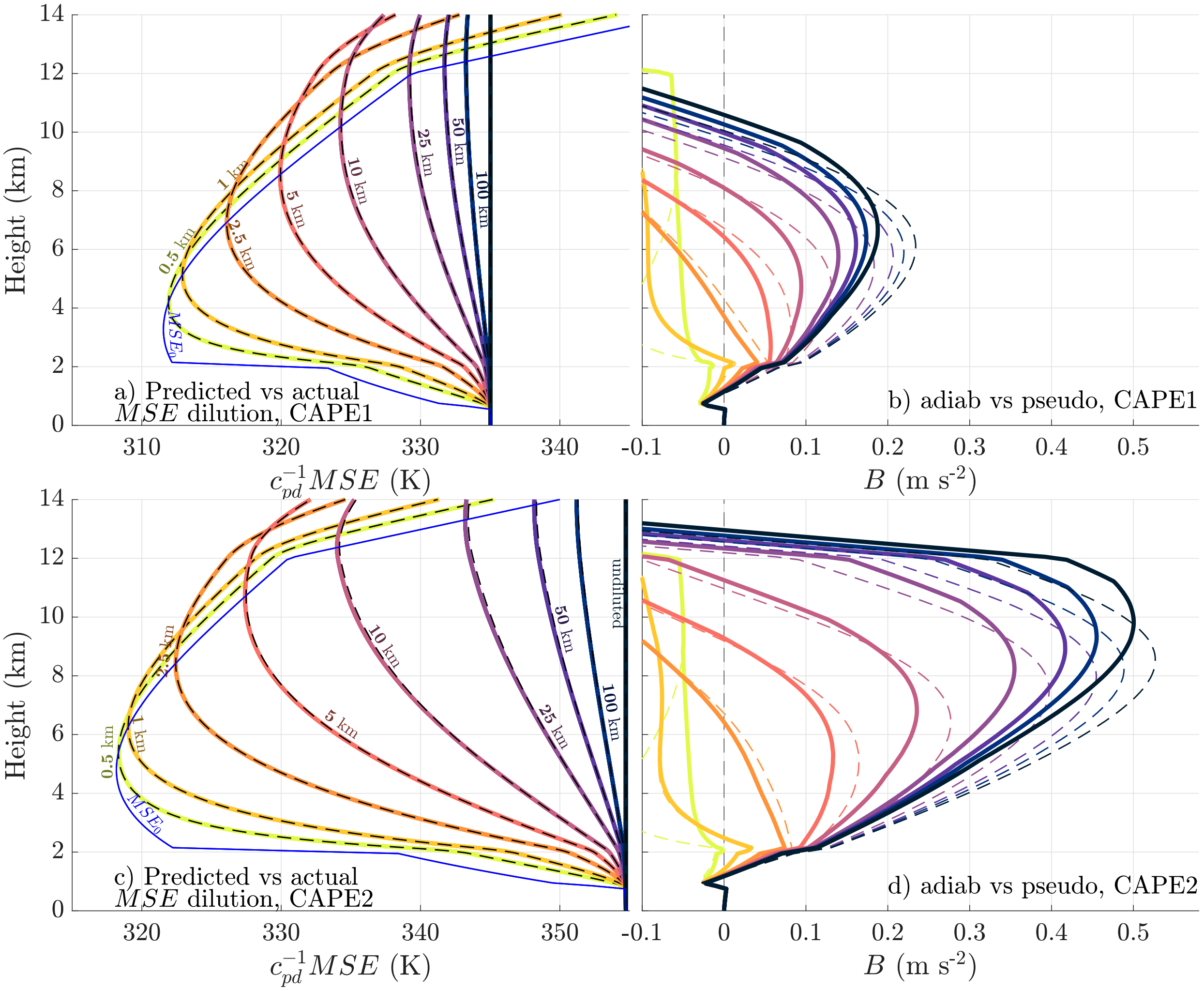

FIG. 6. (a),(c) MSE/c_{pd} (K) computed from T, q_v, and q_t that were predicted by using the P21 adiab formula with nonequilibrium mixed-phase conditions, and with $B = 0$ (thick colored lines; colors correspond to ε^{-1}) vs the analogous quantity predicted by analytically solving the equation $d\text{MSE}/dz = -\varepsilon(\text{MSE} - \text{MSE}_0)$ (dashed black lines). MSE$_0/c_{pd}$ is shown in blue. (b),(d) B (m s^{-2}) predicted using the P21 adiab formula with nonequilibrium mixed-phase conditions and with the B term included (solid lines), and for an analogous pseudo parcel (dashed lines). Results are shown for (top) the CD21 CAPE1 profile and (bottom) the CD21 CAPE2 profile.

which is used to obtain T, and Eq. (38) to obtain q_t. Equation (27) is used to obtain q_v in the isothermal layer and to determine the depth of this layer.

3) Diluted pseudo ascent. In this scenario, Eq. (24) becomes

$$\frac{dT}{dz}_{\text{pseudo,dil}} = -\frac{g}{c_{pd}} \times \frac{\dfrac{B}{g} + 1 + (1 - q_{v,s})\dfrac{L_s Q_M}{R_{m,0} T_0} - \dfrac{c_{pm}}{g}\epsilon_T - \dfrac{L_s}{g}\left[\epsilon_{q_v} - (q_{v,s,i} - q_{v,s,l})\dfrac{\partial \omega}{\partial z}\right]}{\dfrac{c_{pmv}}{c_{pd}} + \dfrac{L_s(q_{v,s,i} - q_{v,s,l})(1 - q_{v,s})}{c_{\text{pd}}}\dfrac{\partial \omega}{\partial T} + (1 - q_{v,s})\dfrac{L_M L_s}{c_{pd} R_v T^2}}, \qquad (42)$$

which is used to obtain T where $\omega = 0$ for $T > 253.15$ K, and $\omega = 1$ for $T \leq 253.15$ K; q_t is set equal to q_v at every vertical step.

The numerical integration and computational logic required to solve these equations follows the methodology used in section 2.

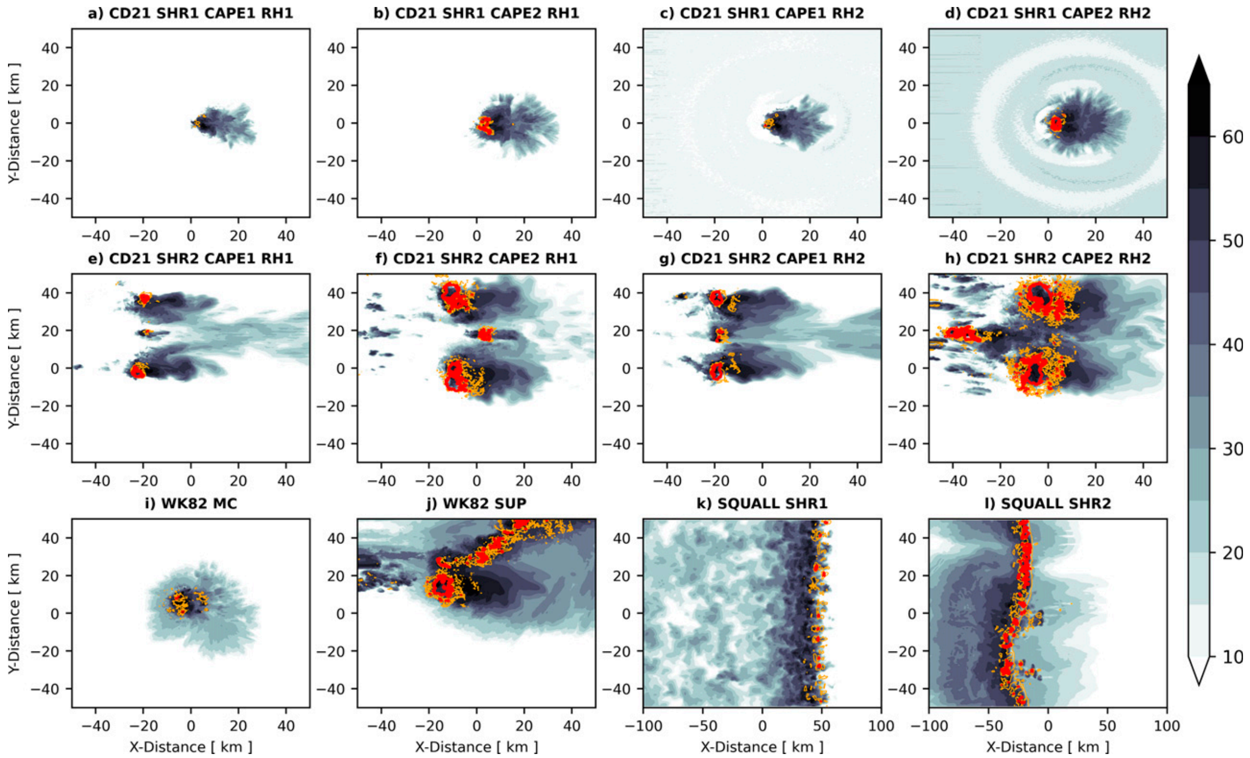

FIG. 7. Plan views of simulated radar reflectivity factor at 1 km (gray shading; dBZ) and maximum column w (orange contours = 15 m s^{-1}; red contours = 30 m s^{-1}) for all simulations. The titles above each panel denote the specific simulation. Results are valid at (a)–(d) 1 h, (e)–(h) 2 h, (i) 1 h, (j) 3 h 10 min, and (k)–(l) 7 h. Note the larger x-axis limits on (k) and (l) compared with all other panels.

a. Numerical model configuration

For this comparison, we simulate a range of modes of deep convective organization to ensure that our formulas are generally valid. These organizational modes include supercells, which often feature nearly undiluted parcel ascent in their cores (Peters et al. 2019, 2020b,c); weak disorganized multicellular clusters, which often have comparatively diluted ascent within their cores (Romps and Kuang 2010; Peters et al. 2020d; Morrison et al. 2020); and squall lines, which feature large p' magnitudes (Peters and Chavas 2021; recall that we neglected p' in our formulas) and dilution rates of updraft cores that are intermediate between supercells and disorganized multicellular clusters (Mulholland et al. 2021).

Our simulations were run with Cloud Model 1 (CM1; Bryan and Fritsch 2002) version 19 with an acoustic time-splitting integration scheme (i.e., option 2 in the namelist). CM1 uses a prognostic equation for θ, and all thermodynamic equations use moisture-dependent heat capacity and temperature-dependent latent heat formulas that are identical to what was used in the section 2 derivations. The majority of our simulations use the double moment microphysics scheme of Morrison et al. (2009, hereafter M09), with the prognostic rimed ice species set to hail. All simulations neglected radiation and surface fluxes, and the top and bottom boundaries were set to "free-slip." Initial and lateral boundary conditions (ICs and LBCs) were specified by a single atmospheric profile, with the addition of perturbations in the ICs to facilitate the development of convection and turbulence. For instance, all simulations included initial random θ perturbations with a maximum amplitude of 0.25 K. To quantify the dilution of air parcels via mixing, a passive tracer with an initial value of 1 kg kg^{-1} was included in the lower part of the domain in the initial conditions. Parcel properties were tracked using trajectories, which were run in-line with model integration, with model variables output onto trajectory locations at each time step.

The first two simulations used the analytic thermodynamic profile of Weisman and Klemp (1982, hereafter WK82), with a $q_{v,\mathrm{sfc}}$ set to 15.7 g kg^{-1} and a middle tropospheric $\mathbb{H}$ of 0.45. These simulations were introduced in Peters et al. (2020b) and were used in Peters et al. (2021) and Peters and Chavas (2021). They used a 100-m isotropic horizontal and vertical grid spacing, and domain dimensions of 100 km in the x and y directions, and 22 km in the z direction, with "open radiative" lateral boundaries (Durran and Klemp 1982). Convection was initialized with a 3-K warm bubble that was centered at the domain center and 500 m above the model surface. Additional details are available in Peters et al. (2020b). In the first of these simulations, the initial u wind profile increased linearly from 0 m s^{-1} at the surface to 6.25 m s^{-1} at a height of 6 km, and remained constant above this height. This simulation (referred to as the "WK82 MC" run) generally had disorganized convection with transient thermal-like updrafts (Fig. 7i). Another nearly identical simulation (referred to as the "WK82

SUP" run), but with a u wind increase to 37.5 m s^{-1} at 6 km produced a sustained supercell updraft (Fig. 7j). The passive tracer layer was 800 m deep in these simulations, and 1000 trajectories were run though each of these simulations [details of these trajectories are available in Peters and Chavas (2021)]. We refer to these simulations collectively as the WK82 runs.

The second set of simulations were similar to the WK82 runs, but with the following differences. Four simulations used the CD21 CAPE1 profile with either a 7.5 m s^{-1} increase in u wind from the surface to 6 km (SHR1), or a 30 m s^{-1} increase over this depth (SHR2), and either $\mathbb{H} = 0.45$ (RH1) or $\mathbb{H} = 0.85$ (RH2) above 2 km. Another set of four simulations used the CD21 CAPE2 profile with the same set of wind and $\mathbb{H}$ combinations. As in the case of the WK82 simulations, the SHR1 simulations generally produced disorganized convection (Figs. 7a–d), whereas the SHR2 simulations produced supercells (Figs. 7e–h). These simulations were initialized with 10 000 trajectories, and with the initial passive tracer layer confined to the 650-m (CD21 CAPE1 runs) and 850-m (CD21 CAPE2 runs) constant MSE layers. We refer to these simulations collectively as the CD21 runs, with RH, SHR, and CAPE specifiers to refer to specific profiles. To evaluate the sensitivity to microphysics, the four CD21 SHR2 simulations were rerun with the NOAA National Severe Storms Laboratory (NSSL) double-moment microphysics scheme (Mansell et al. 2010) in lieu of the M09 scheme, which includes prognostic equations for hail and graupel.

The final set of simulations originated from Mulholland et al. (2021) and were further used in Peters and Chavas (2021). The initial thermodynamic profile was a modified version of the WK82 profile with a $q_{v,\mathrm{sfc}}$ of 13.7 g kg^{-1} in the boundary layer and $\mathbb{H} = 0.45$ above 2.5 km. One simulation featured moderate vertical wind shear, and the other featured strong vertical wind shear [for details, see Mulholland et al. (2021)]. In these simulations, a cold pool was included in the ICs rather than a warm bubble, resulting in the formation of a squall line. The domain dimensions were 99 km in the y direction and 420 km in the x direction, with open radiative LBCs in the x direction and periodic LBCs in the y direction. The grid spacing was isotropic at 250 m in the horizontal and vertical. Simulations were initialized with 1000 trajectories, and the initial passive tracer was confined to the lowest 1.5 km. We refer to these simulations collectively as the "SQUALL" line runs (Figs. 7k–l).

b. *Analysis methods*

To compare our formulas to trajectories in simulations, we first introduce an equation that predicts the passive tracer concentration C in conjunction with T and q_t in our lapse rate formulas. Setting $\psi = C$ in Eq. (40), $C_0 = 0$ kg kg^{-1}, and $C_b = 1$ kg kg^{-1} at the height of the top of the passive tracer layer z_{pt}, reduces Eq. (40) to

$$C = e^{-\varepsilon(z - z_{\mathrm{pt}})}. \tag{43}$$

This equation describes the dilution at a given height of a parcel that obeys our lapse rate equations. Thus, our lapse rate equations and Eq. (43) give us predicted profiles of B, q_t, and C for a given value of ε.

Next, we identified continuous time periods of vertical velocity $w > 0.5$ m s^{-1} along each trajectory that also contained the maximum w achieved along that trajectory. Using these continuous time periods, we vertically interpolated trajectory B, q_t, and C, onto a regular height grid at intervals of 100 m. To obtain the profiles of B and q_t from simulations that were compared with predicted profiles, we binned points from trajectories whose C fell within 0.01 kg kg^{-1} of the value predicted by Eq. (43) at each 100-m interval in the vertical. This ensures that we are comparing similarly diluted parcels in the numerical simulations with predictions from our lapse rate formulas. In this procedure, we have implicitly assumed that the parcels in the simulation experienced constant dilution rates as they rose from their origin heights, where they all share similar or identical starting MSE. We then computed vertical profiles of the 5th and 95th percent confidence bounds on the average B and q_t for the points within each bin based on a Student's t test. At each height, these confidence bounds represent the range of B and q_t on trajectories that experienced the same average mixing rate ε along their ascent as the parcels in the predicted profiles.

For an arbitrary predicted quantity ψ_{pred}, we quantify errors via the following root-mean-square error (RMSE) formula:

$$\mathrm{RMSE} \equiv 100\sqrt{\frac{\displaystyle\int_{z=z_1}^{z=z_2}(\psi_{\mathrm{pred}} - \psi_{\mathrm{traj}})^2 dz}{\displaystyle\int_{z=z_1}^{z=z_2}\psi_{\mathrm{traj}}^2 dz}}, \tag{44}$$

where ψ_{traj} is the mean of all ψ from trajectories binned within a given 100-m interval, and z_1 and z_2 are the bottom and top of the layer over which errors are being assessed. This formula yields percentage errors, with small values (i.e., <20%) indicating accurate predictions, and large values (i.e., >100%) indicating inaccurate predictions. We compare predicted versus trajectory profiles in each simulation for $\varepsilon^{-1} = 5$, 10, 25, 50, 100, and ∞ km (undiluted).

c. *Comparison of lapse rate formulas with numerical model trajectories*

Our objectives in the comparison between predictions from our lapse rate formulas to the simulations are as follows:

- Determine whether predicted CAPE[1] and profiles of B and q_t by our lapse rate formulas compare against profiles from trajectories for both undiluted and diluted ascent, and whether adiab irev, adiab rev, or pseudo ascent gives the best correspondence.
- Quantify the error dependencies on convective mode and ε using our RMSE definition.
- Compare the quantitative errors between adiab irev, adiab rev, and pseudo ascent to address our hypothesis.

1) SUBJECTIVE COMPARISON

We begin by qualitatively comparing vertical profiles of B (Figs. 8a–f) and q_t, q_i, and q_l (Figs. 8g–l) from the WK82

---

[1] CAPE $\equiv \int_{z=\mathrm{LFC}}^{z=\mathrm{EL}} B\,dz$ (where LFC is the level of free convection and EL is the equilibrium level).

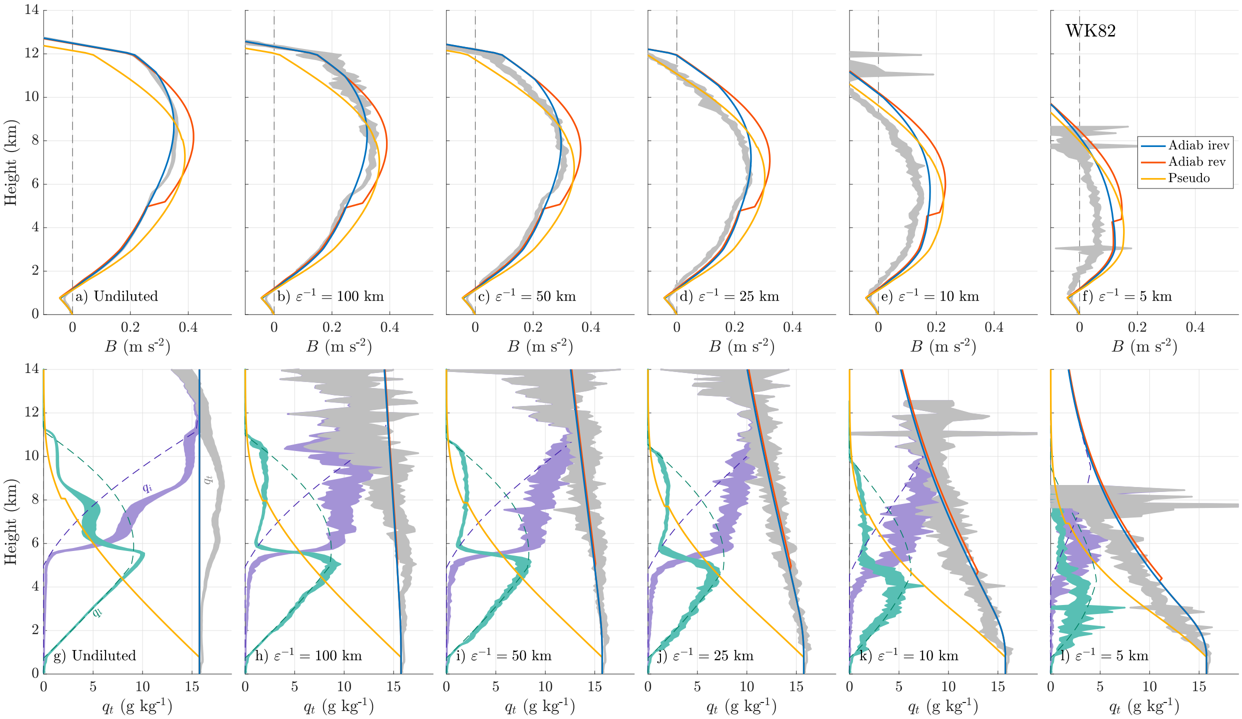

FIG. 8. (top) B (m s^{-2}) in the WK82 simulations for an adiab irev parcel that experiences nonequilibrium mixed-phase conditions (blue lines), for an adiab rev parcel (red lines), and for a pseudo parcel (yellow lines). The 5th–95th percentile confidence bounds on the average B for parcels in simulations that experienced dilution consistent with ε are shown as a gray area. Each panel corresponds to the ε^{-1} indicated in the panel label. (bottom) As in the top panels, but showing q_t (g kg^{-1}). Additionally shown in the bottom row are ranges for q_l (teal shading) and q_i (violet shading), with respective predictions from the mixed-phase parameterization used in the abiab irev predictions (teal and violet dashed lines).

simulation, with predictions by the lapse rate formulas from the combined WK82 SUP and MC simulation as a representative example. The results shown here exemplify the general behaviors among the other simulations.

In the case of undiluted (Fig. 8a) and moderately diluted (Figs. 8b,c) simulated parcels, the adiab irev, adiab rev, and pseudo predictions of B all capture the qualitative structure of the profiles of B from the simulations. However, there are some notable differences among the three predictions. Pseudo predictions generally overestimate B below 8 km, and generally underestimate B above 8 km. In contrast, both adiab rev and irev predictions very closely match the simulated profiles below the freezing level, which occurs at approximately 5 km. Above the freezing level, adiab rev predictions generally overpredict B, whereas adiab irev predictions remain in close correspondence with the simulated profiles all the way from the freezing level to the EL. In the case of moderately-to-strongly diluted parcels (Figs. 8d–f), all three of the profiles slightly overpredict B, with the adiab irev B profile providing the closest correspondence with the simulated B profile below 8 km, and the pseudo B profile providing the closest correspondence with the simulated B profile above 8 km and below the EL.

Profiles of simulated q_t for all dilution rates show a close correspondence with adiab irev and rev q_t (Figs. 8g–l), whereas pseudo q_t substantially underpredicts q_t. Profiles of q_l and q_i from the simulation show a more abrupt transition from liquid to ice at the freezing level than is portrayed in the adiab irev formula (Figs. 8g–l), albeit with parcels in the simulations retaining a small amount of supercooled liquid water above the freezing level. This contrasts somewhat with the more gradual transition portrayed by the adiab irev parcel. Hence, the behavior of the simulations appears to lie somewhere between that of the adiab irev and rev lapse rate formulas. This is also consistent with the thin layer above the freezing level where there is a brief, but rapid increase in B (Figs. 8a–f) that is not predicted by adiab irev, but smaller in magnitude than that predicted by adiab rev.

Next, we investigate vertical profiles of errors across all simulations (Fig. 9) to uncover any dependencies of errors on height and/or convective mode. In general, errors from the adiab irev and rev formulas in predicting B were less than half that of the pseudo formula below 6 km (Figs. 9a–l). The only notable exceptions to this trend were in the CD21 SHR1 CAPE1 RH1 (Fig. 9a) and RH2 (Fig. 9c) simulations, where the pseudo prediction outperformed the adiab predictions. However, there were far fewer parcels that ascended through updrafts in these two simulations, and the parcels that did ascend through updrafts were all strongly diluted. Thus, it is unclear whether the different behavior in these simulations

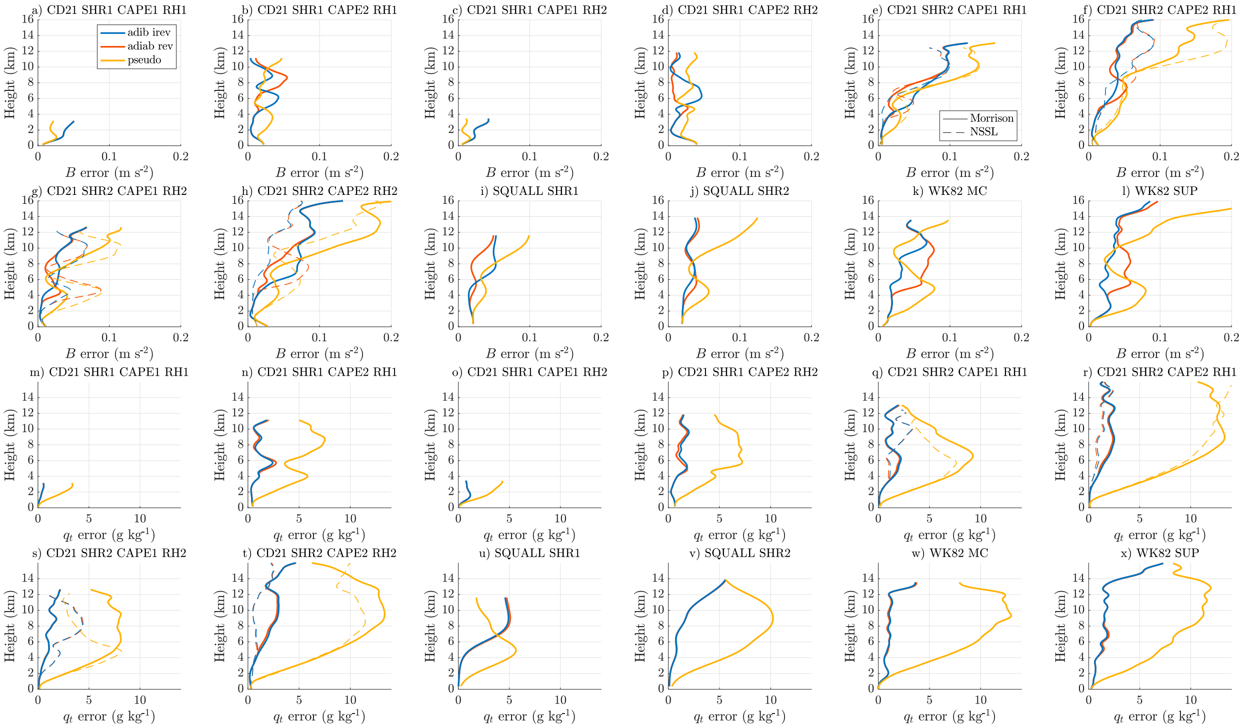

FIG. 9. Vertical profiles of the magnitude of errors in predictions of simulated (a)–(l) B (m s^{-2}) and (m)–(x) q_t (g kg^{-1}) using the adiab irev formula (blue), the adiab rev formula (red), and the pseudo formula (yellow). At each height, errors are averaged over all simulated trajectories. Solid lines correspond to the simulations run with M09 microphysics, and dashed lines correspond to simulations run with the NSSL microphysics. Each panel corresponds to the simulation listed in the panel title.

compared to the other simulations reflects a dependency of errors in prediction on convective mode. Errors associated with the pseudo formula were generally comparable to, or slightly less than, the adiab formulas at midlevels (i.e., in the 6–10-km range); however, pseudo errors were once again much larger than the adiab formulas aloft (i.e., above 8 km).

Across all simulations adiab predictions of q_t incurred far smaller errors than predictions of q_t using the pseudo formula (Figs. 9m–x). In general, this subjective assessment points to an advantage of the adiab rev and irev formulas over the pseudo formulas in predicting B, particular at low and upper levels, and in predicting q_t at all levels. This is an important result, given that low-level B may substantially influence CIN and LFC height calculations, and potentially influences tornadogenesis (Brown and Nowotarski 2019; Coniglio and Parker 2020).

The NSSL simulations (Figs. 9e–h,q–t) display nearly identical error patterns to the M09 scheme, suggesting that the trends in Fig. 9 are not a unique artifact of the M09 microphysics scheme.

2) QUANTITATIVE COMPARISONS

We quantitatively assess our formulas in two ways. First, we compute the RMSE for B, q_t, and CAPE, averaged (without weighting) over all ε values for each simulation. Note that in the case of CAPE, there is a single predicted value and a single simulated value, and RMSE is defined as $100\left(\left|\mathrm{CAPE}_{\mathrm{pred}} - \mathrm{CAPE}_{\mathrm{traj}}\right|/\mathrm{CAPE}_{\mathrm{traj}}\right)$. Second, we averaged RMSE over all simulations for each ε value, allowing us to characterize the dependency of the accuracy of predictions on ε.

In general, B RMSE averaged over all ε was smallest for the adiab irev predictions, aside from the CD21 SHR1 CAPE1 simulations, and largest for the pseudo predictions (Fig. 10a). In general, pseudo predictions of B produced roughly 20% larger errors than adiab irev predictions. Note that trajectories only made it above 2 km in the CD21 SHR1 CAPE1 simulations for $\varepsilon^{-1} < 25$ km. In other words, only highly diluted parcels were present in the updrafts of these simulations. Since our formulas generally performed worse with smaller ε^{-1}, it is possible that the better performance of the pseudo predictions over the adiab irev predictions in the CD21 SHR1 CAPE1 simulations is biased by this fact. Similar patterns were present for CAPE predictions, although the difference among the methods were smaller and less consistent than in the case of B (Fig. 10b). In general, RMSE for adiab irev and rev q_t were far smaller than that for pseudo (Fig. 10c); this difference was relatively small only for the CD21 SHR1 CAPE1 simulations. It is possible that the CD21 SHR1 CAPE1 simulations behaved in a manner closer to pseudo ascent than that of the other simulations, but this pattern does not appear to be coherent among all disorganized

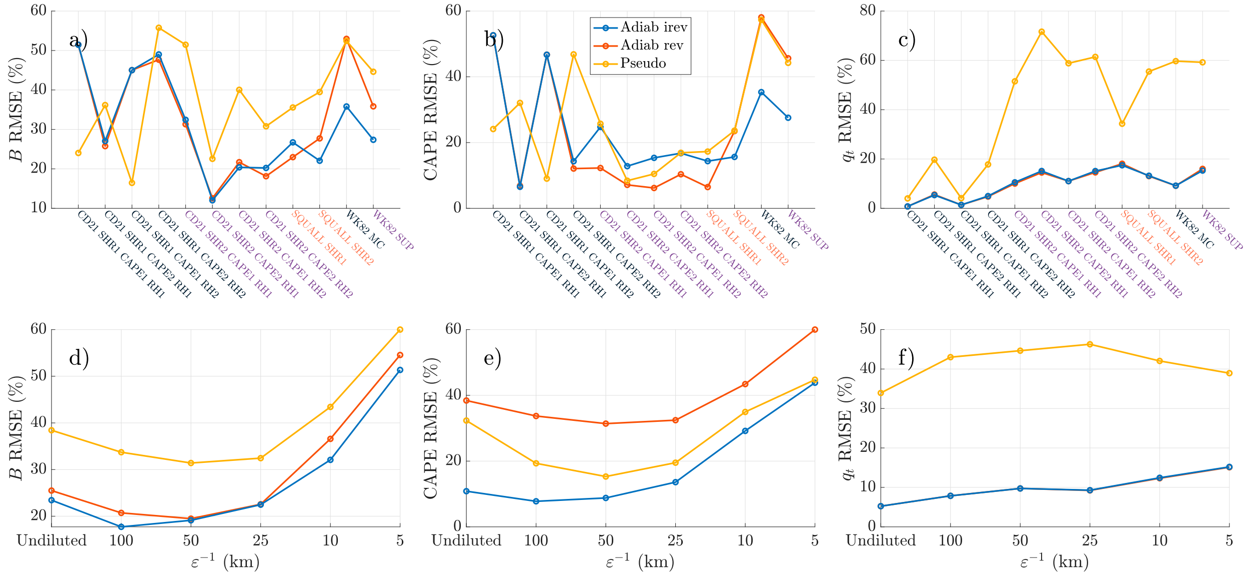

FIG. 10. (top) RMSE (%; y axis) averaged over all ε for (a) B, (b) CAPE, and (c) q_t for the simulations indicated in the x-axis labels. Black labels correspond to the multicellular convective mode, purple labels correspond to supercells, and orange labels correspond to squall lines. (bottom) RMSE (%; y axis) averaged over all simulations as a function of ε^{-1} (km; x axis) for (d) B, (e) CAPE, and (f) q_t. In all panels: adiab irev predictions are shown by blue lines and dots, adiab rev predictions by red lines and dots, and pseudo predictions by yellow lines and dots. Note that the y-axis limits are different among the different panels. Also note that the $\varepsilon^{-1} = 5$ km category was excluded from the SQUALL simulations because of a spuriously low sample size (only 10 trajectories) in this category.

multicellular convection. For instance, the CD21 SHR1 CAPE2 and the WK82 MC simulations showed behavior that was clearly closer to adiab irev, in a similar manner to the supercell and squall line simulations. When averaged over all simulations, it is apparent that adiab predictions, and adiab irev in particular, perform the most skillfully for nearly all ε, and for B, CAPE, and q_t (Figs. 10d–f).

d. *Computational considerations*

Traditional methods for computing CAPE or ECAPE use implicit numerical integration, wherein an iterative procedure is required to solve for T at each vertical level. From our experience, this procedure results in a computational bottleneck when computing CAPE for many locations in large datasets. The explicit vertical integration of lapse rate equations offers a computational advantage over these implicit methods, requiring much fewer operations at each vertical level. This is particularly true in the case of MSE − IB as a conserved quantity because IB itself requires integration of buoyancy along the parcel path; hence, buoyancy must be calculated incrementally at high vertical resolution as part of an implicit scheme, similar to an explicit scheme. To demonstrate this computational advantage, we compare vertical profiles of adiab irev B computed using an explicit Euler integration scheme with a vertical grid spacing Δz ranging from 500 to 1 m, to implicit solutions for adiab irev B using a Crank–Nicholson integration scheme. Iterative solutions for T were computed in Matlab using the fzero function (Brent 1973) with the T at the next lowest grid height as an initial guess. Errors were assessed relative to an implicit solution with $\Delta z = 1$ m, which we call the "benchmark" prediction.

A subjective comparison of the explicit predictions with the benchmark prediction reveals that the explicit solutions reproduce the qualitative B profile with all of the Δz considered here (Fig. 11a). RMSE of the explicit solutions generally decrease monotonically with decreasing Δz, dropping below 1% for $\Delta z < 100$ m (Fig. 11b). Commensurately, computation time for both explicit and implicit methods increased exponentially as Δz decreased (Fig. 11c). Importantly, the computation time for the explicit scheme was consistently a factor of 3.5–4 smaller than that of the implicit scheme (gray line in Fig. 11c), demonstrating the computational advantage of the explicit scheme over the implicit. In practice, one may have inconsistent vertical spacing of grid points among data, and interpolation to a common grid may be necessary before computing CAPE. Adding this step to the explicit vertical integration scheme (not shown) adds a negligible amount of computation time for this method.

4. Summary, conclusions, and discussion

To improve the accuracy of calculations that rely on parcel theory, such as the computation of CAPE, we have derived general lapse rate formulas for subsaturated and saturated parcel ascent. The starting point for these derivations is an expression for the conservation of energy, rather than an expression for the conservation of moist entropy. As was pointed out by R15, basing our derivation on conservation of

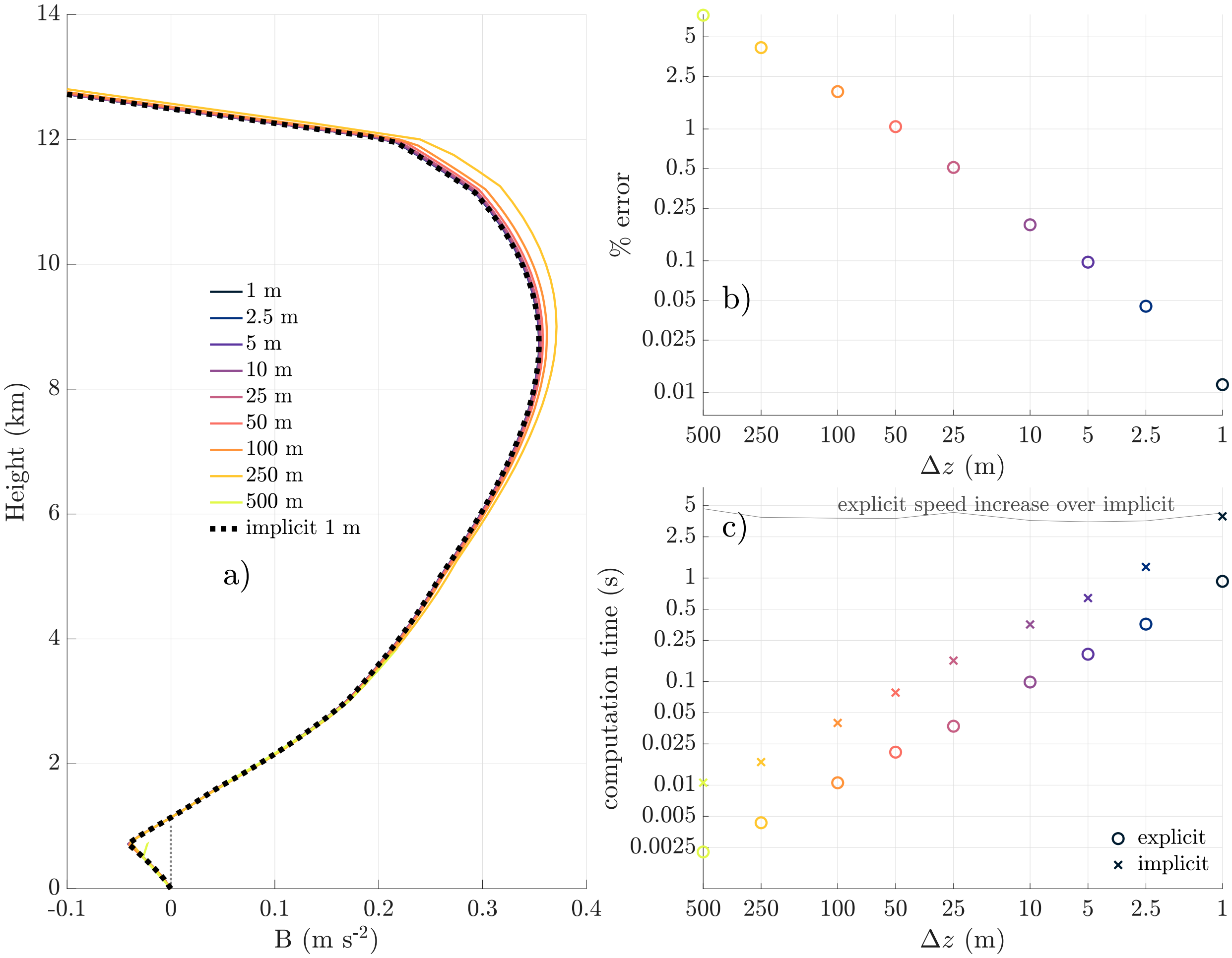

FIG. 11. (a) Profiles of B (m s^{-2}) predicted using the explicit Euler integration scheme with the adiab irev formula (colored lines) with a vertical grid spacing Δz ranging from 500 to 1 m. The B predicted with an implicit Crank–Nicholson scheme with a 1-m Δz is shown as a black dotted line, and is used as "truth" for error calculations in (b). (b) RMSE [circles with a color scheme matching (a); %; y axis] of B predicted via explicit integration of the adiab irev formula as a function of Δz (x axis). (c) Computation time (s; y axis) required to compute a 20-km profile of B using the explicit adiab irev formula (circles), the implicit Crank–Nicholson scheme (x marks), and the ratio of implicit to explicit computation time (gray line) as a function of Δz (x axis).

energy allows us to escape errors related to entropy sources when nonequilibrium mixed-phase processes occur. These new formulas use fewer assumptions than past formulas, and are shown to exactly conserve MSE − IB for a general adiabatic parcel, and moist entropy for a reversibly lifted adiabatic parcel (both requirements for an adiabatic parcel). These formulas also incorporate terms that account for the mixing of a parcel with its surroundings, and are therefore suitable for computing quantities such as ECAPE. Finally, energy-based formulas are straightforward to interpret conceptually in terms of exchanges of different forms of parcel energy.

We first compared these new formulas with previous lapse rate formulas for undiluted parcel ascent and identified inconsistencies in previous derivations that lead to errors. We then compared the B and q_t profiles predicted by our formulas to the analogous quantities along trajectories in simulations of various modes of deep moist convection. Our conclusions are as follows:

- Predictions of B and q_t from our formulas reproduce well profiles from simulated trajectories for weakly and moderately diluted parcels. Correspondence degrades for strongly diluted parcels, likely due to complicating factors such as the vertical exchanges of hydrometeors through precipitation.
- Predictions with our formulas of trajectory properties show the best correspondence and most quantitative skill when adiabatic irreversible or reversible parcel ascent is assumed, and when q_t is diluted at the same entrainment rate that is used to dilute other parcel properties.

The better correspondence between adiabatic, rather than pseudoadiabatic, parcel calculations and simulations makes a degree of intuitive sense. For instance, precipitation from parcels high within the cloud falls into parcels that are lower in the cloud, as was postulated by Xu and Emanuel (1989). So even if parcels are precipitating out all condensate that originates from their initial stock of water vapor, they will experience a condensate source from adjacent parcels above that are also precipitating, and thus would be expected to have significant condensate as they rise. So in the cases of nearly undiluted simulated parcels that were examined here, the parcels likely do not retain all of their original stock of water that they begin with before their ascent. Rather, they are continuously losing and gaining water molecules at rates that are nearly in balance, so that their q_t may only change gradually.

Based on the second conclusion, we argue that CAPE computed from adiabatic parcel ascent is more relevant to the behavior of real moist convection than CAPE computed from pseudoadiabatic parcel ascent. Thus, computational routines that currently compute CAPE pseudoadiabatically should consider switching to adiabatic calculations. Because there are often substantial differences between adiabatic and pseudoadiabatic buoyancy in the lower troposphere, pseudoadiabatic and adiabatic CAPE calculations may yield relatively large differences in CIN and LFC height calculations. Future work is planned to investigate the impact of computing CAPE with adiabatic assumptions in a large database of observed storm environments.

An obvious and important caveat to this work is that our conclusions are only as good as the microphysical parameterization used in our LES. In situ microphysical observations of clouds, coupled with radiosonde observations to observe clouds' nearby environments, are necessary to observationally validate our hypothesis, and should also be examined in future work.

Acknowledgments. We thank Tristan Abbott, Chris Holloway, and a third anonymous reviewer for their comments on an earlier version of this manuscript. We also thank Robert Warren for pointing out derivation errors in an earlier version of this article that were fixed during production. J. Peters's and J. Mulholland's efforts were supported by National Science Foundation (NSF) Grants AGS-1928666 and AGS-1841674 and the Department of Energy Atmospheric System Research (DOE ASR) Grant DE-SC0000246356. D. Chavas was supported by NSF Grant AGS-1648681.

Data availability statement. All scripts and namelists used to generate the data for this study are available via Figshare at https://figshare.com/articles/dataset/Untitled_Item/14515560.

APPENDIX A

The Definition of Enthalpy

We derive the definition of (specific) enthalpy, k, given by Eq. (1). The derivation follows that of Emanuel (1994, p. 118) except for enthalpy defined in terms of mass fractions rather than mixing ratios and including ice. The total enthalpy content of a parcel is equal to the sum of the enthalpy content of its constituents:

$$Mk = M_d k_d + M_v k_v + M_l k_l + M_i k_i, \tag{A1}$$

where M_x corresponds to the mass of a constituent x and M is the total mass. Dividing through by M and using the definition of mass fraction yields

$$k = (1 - q_t)k_d + q_v k_v + q_l k_l + q_i k_i. \tag{A2}$$

The latent heat of phase change is defined as the enthalpy difference between the final and initial phase: $L_v(T) = k_v - k_l$ for vaporization and $L_i(T) = k_l - k_i$ for melting. Using these equations, Eq. (A2) may be rewritten as

$$k = (1 - q_t)k_d + q_t k_l + L_v q_v - L_i q_i. \tag{A3}$$

Finally, using the definitions of enthalpy for dry air, $k_d = c_p T$, and liquid water, $k_l = c_l T$, and rearranging yields Eq. (1).

APPENDIX B

Exact Formula for *B* when *p*′ = 0

Writing ρ as the sum of the partial densities ρ_d from dry air, ρ_v from water vapor, and ρ_c from condensate, gives

$$\rho = \rho_d + \rho_v + \rho_c. \tag{B1}$$

Using the ideal gas law, noting that $\rho_c = (q_t - q_v)\rho$, setting $p = p_0$, and rearranging gives

$$\rho = \frac{1}{R_d T}\frac{p_0 + (\varphi - 1)\mathbb{E}}{1 - q_t + q_v}, \tag{B2}$$

where $\varphi \equiv R_d/R_v$. In noting that $\mathbb{E} = q_v p_0/(\varphi - q_t\varphi + q_v)$ if condensate volume is neglected, we arrive at the following definition of density temperature T_ρ:

$$T_\rho = T\left(1 - q_t + \frac{q_v}{\varphi}\right). \tag{B3}$$

This definition of T_ρ exactly satisfies the equation

$$p_0 = \rho R_d T_\rho. \tag{B4}$$

Following the derivation of Eq. (B3), the density temperature $T_{\rho,0}$ is

$$T_{\rho,0} = T\left[1 + (\varphi^{-1} - 1)q_{v,0}\right]. \tag{B5}$$

Using these definitions, it can be shown that

$$B = -g\frac{\rho'}{\rho} = g\frac{T_\rho - T_{\rho,0}}{T_{\rho,0}} \tag{B6}$$

is exact, so long as $p' = 0$.

APPENDIX C

Expansion of dq_v/dz

We begin by taking d/dz of Eq. (20) and applying the chain rule, to obtain

$$\frac{dq_{v,s}}{dz} = (q_{v,s,i} - q_{v,s,l})\left(\frac{\partial\omega}{\partial T}\frac{dT}{dz} + \frac{\partial\omega}{\partial z}\right) + (1-\omega)\frac{dq_{v,s,l}}{dz} + \omega\frac{dq_{v,s,i}}{dz}. \tag{C1}$$

In further taking d/dz of Eqs. (11) and (12) with $p = p_0$ and applying the chain rule, we obtain

$$\frac{dq_{v,s,l}}{dz} = -\frac{q_{v,s,l}}{1-q_t}\epsilon_{q_t} - \frac{p_0}{p_0 - \mathbb{E}_{s,l}}\left(\frac{q_{v,s,l}}{p_0}\frac{dp_0}{dz} - \frac{q_{v,s,l}}{\mathbb{E}_{s,l}}\frac{d\mathbb{E}_{s,l}}{dz}\right), \text{ and} \tag{C2}$$

$$\frac{dq_{v,s,i}}{dz} = -\frac{q_{v,s,i}}{1-q_t}\epsilon_{q_t} - \frac{p_0}{p_0 - \mathbb{E}_{s,i}}\left(\frac{q_{v,s,i}}{p_0}\frac{dp_0}{dz} - \frac{q_{v,s,i}}{\mathbb{E}_{s,i}}\frac{d\mathbb{E}_{s,i}}{dz}\right). \tag{C3}$$

Using algebra and the ideal gas law, we obtain

$$\frac{p_0}{p_0 - \mathbb{E}_{s,l}} = \frac{\varphi - \varphi q_t + q_{v,s}}{\varphi - \varphi q_t + q_{v,s} - q_{v,s,l}} = \frac{1}{1 - \mathbb{Q}_{v,s,l}}, \text{ and} \tag{C4}$$

$$\frac{p_0}{p_0 - \mathbb{E}_{s,i}} = \frac{\varphi - \varphi q_t + q_{v,s}}{\varphi - \varphi q_t + q_{v,s} - q_{v,s,i}} = \frac{1}{1 - \mathbb{Q}_{v,s,i}}, \tag{C5}$$

where $\mathbb{Q}_{v,s,l} \equiv q_{v,s,l}/(\varphi - \varphi q_t + q_{v,s})$ and $\mathbb{Q}_{v,s,i} \equiv q_{v,s,i}/(\varphi - \varphi q_t + q_{v,s})$. Combining Eqs. (C1), (C2), (C3), (C5), (7), and (8), and noting that $d\mathbb{E}_{s,l}/dz = (d\mathbb{E}_{s,l}/dT)dT/dz$ and $d\mathbb{E}_{s,i}/dz = (d\mathbb{E}_{s,i}/dT)dT/dz$, gives

$$\begin{aligned}\frac{dq_{v,s}}{dz} &= (q_{v,s,i} - q_{v,s,l})\left(\frac{\partial\omega}{\partial T}\frac{dT}{dz} + \frac{\partial\omega}{\partial z}\right) - \frac{q_{v,s}}{1-q_t}\epsilon_{q_t} \\ &\quad - \frac{Q_M}{p_0}\frac{dp_0}{dz} + \frac{L_M}{R_v T^2}\frac{dT}{dz},\end{aligned} \tag{C6}$$

where

$$Q_M \equiv \left[(1-\omega)\frac{q_{v,s,l}}{1-\mathbb{Q}_{v,s,l}} + \omega\frac{q_{v,s,i}}{1-\mathbb{Q}_{v,s,i}}\right], \text{ and}$$

$$L_M \equiv \left[(1-\omega)L_v\frac{q_{v,s,l}}{1-\mathbb{Q}_{v,s,l}} + \omega(L_v + L_i)\frac{q_{v,s,i}}{1-\mathbb{Q}_{v,s,i}}\right].$$

The M subscript stands for "mixed," indicating that this latent heat term is expressed as a function of other terms that result from the presence of mixed-phase condensate in thermodynamic disequilibrium. In the situation where $\omega = 0$ or $\omega = 1$, it can be shown that

$$Q_M = q_{v,s}\left[1 + \frac{q_{v,s}}{\varphi(1-q_t)}\right], \text{ and}$$

$$L_M = q_{v,s}\left[1 + \frac{q_{v,s}}{\varphi(1-q_t)}\right]L_s.$$

REFERENCES

Arakawa, A., and W. H. Schubert, 1974: Interaction of a cumulus cloud ensemble with the large-scale environment, part I. *J. Atmos. Sci.*, **31**, 674–701, https://doi.org/10.1175/1520-0469(1974)031<0674:IOACCE>2.0.CO;2.

Bakhshaii, A., and R. Stull, 2013: Saturated pseudoadiabats—A noniterative approximation. *J. Appl. Meteor. Climatol.*, **52**, 5–15, https://doi.org/10.1175/JAMC-D-12-062.1.

Betts, A. K., 1974: Further comments on "A comparison of the equivalent potential temperature and the static energy." *J. Atmos. Sci.*, **31**, 1713–1715, https://doi.org/10.1175/1520-0469(1974)031<1713:FCOCOT>2.0.CO;2.

Blumberg, W. G., K. T. Halbert, T. A. Supinie, P. T. Marsh, R. L. Thompson, and J. A. Hart, 2017: SHARPpy: An open-source sounding analysis toolkit for the atmospheric sciences. *Bull. Amer. Meteor. Soc.*, **98**, 1625–1636, https://doi.org/10.1175/BAMS-D-15-00309.1.

Bohren, C. F., and B. A. Albrecht, 1998: *Atmospheric Thermodynamics.* Oxford University Press, 402 pp.

Bolton, D., 1980: The computation of equivalent potential temperature. *Mon. Wea. Rev.*, **108**, 1046–1053, https://doi.org/10.1175/1520-0493(1980)108<1046:TCOEPT>2.0.CO;2.

Brent, R., 1973: *Algorithms for Minimization without Derivatives.* Prentice Hall, 195 pp.

Brown, M., and C. J. Nowotarski, 2019: The influence of lifting condensation level on low-level outflow and rotation in simulated supercell thunderstorms. *J. Atmos. Sci.*, **76**, 1349–1372, https://doi.org/10.1175/JAS-D-18-0216.1.

Bryan, G. H., and J. M. Fritsch, 2002: A benchmark simulation for moist nonhydrostatic numerical models. *Mon. Wea. Rev.*, **130**, 2917–2928, https://doi.org/10.1175/1520-0493(2002)130<2917:ABSFMN>2.0.CO;2.

——, and ——, 2004: A reevaluation of ice–liquid water potential temperature. *Mon. Wea. Rev.*, **132**, 2421–2431, https://doi.org/10.1175/1520-0493(2004)132<2421:AROIWP>2.0.CO;2.

Chavas, D. R., and D. T. Dawson, 2021: An idealized physical model for the severe convective storm environmental sounding. *J. Atmos. Sci.*, **78**, 653–670, https://doi.org/10.1175/JAS-D-20-0120.1.

Coniglio, M. C., and M. D. Parker, 2020: Insights into supercells and their environments from three decades of targeted radiosonde observations. *Mon. Wea. Rev.*, **148**, 4893–4915, https://doi.org/10.1175/MWR-D-20-0105.1.

Davies-Jones, R., 2002: Linear and nonlinear propagation of supercell storms. *J. Atmos. Sci.*, **59**, 3178–3205, https://doi.org/10.1175/1520-0469(2003)059<3178:LANPOS>2.0.CO;2.

——, 2003: An expression for effective buoyancy in surroundings with horizontal density gradients. *J. Atmos. Sci.*, **60**, 2922–2925, https://doi.org/10.1175/1520-0469(2003)060<2922:AEFEBI>2.0.CO;2.

——, 2008: An efficient and accurate method for computing the wet-bulb temperature along pseudoadiabats. *Mon. Wea. Rev.*, **136**, 2764–2785, https://doi.org/10.1175/2007MWR2224.1.

Durran, D. R., and J. B. Klemp, 1982: On the effects of moisture on the Brunt-Väisälä frequency. *J. Atmos. Sci.*, **39**, 2152–2158, https://doi.org/10.1175/1520-0469(1982)039<2152:OTEOMO>2.0.CO;2.

Emanuel, K. A., 1994: *Atmospheric Convection.* Oxford University Press, 588 pp.

Khairoutdinov, M., and D. A. Randall, 2003: Cloud resolving modeling of the ARM summer 1997 IOP: Model formulation, results, uncertainties, and sensitivities. *J. Atmos. Sci.*, **60**, 607–625, https://doi.org/10.1175/1520-0469(2003)060<0607:CRMOTA>2.0.CO;2.

Kuang, Z., and C. S. Bretherton, 2006: A mass flux scheme view of a high-resolution simulation of a transition from shallow to deep cumulus convection. *J. Atmos. Sci.*, **63**, 1895–1909, https://doi.org/10.1175/JAS3723.1.

Mansell, E. R., C. L. Ziegler, and E. C. Bruning, 2010: Simulated electrification of a small thunderstorm with two-moment bulk microphysics. *J. Atmos. Sci.*, **67**, 171–194, https://doi.org/10.1175/2009JAS2965.1.

Marquet, P., 2016: Comments on "MSE minus CAPE is the true conserved variable for an adiabatically lifted parcel." *J. Atmos. Sci.*, **73**, 2565–2575, https://doi.org/10.1175/JAS-D-15-0299.1.

Moncrieff, M. W., and M. J. Miller, 1976: The dynamics and simulation of tropical cumulonimbus and squall lines. *Quart. J. Roy. Meteor. Soc.*, **102**, 373–394, https://doi.org/10.1002/qj.49710243208.

Morrison, H., 2017: An analytic description of the structure and evolution of growing deep cumulus updrafts. *J. Atmos. Sci.*, **74**, 809–834, https://doi.org/10.1175/JAS-D-16-0234.1.

——, G. Thompson, and V. Tatarskii, 2009: Impact of cloud microphysics on the development of trailing stratiform precipitation in a simulated squall line: Comparison of one- and two-moment schemes. *Mon. Wea. Rev.*, **137**, 991–1007, https://doi.org/10.1175/2008MWR2556.1.

——, J. M. Peters, A. C. Varble, W. M. Hannah, and S. E. Giangrande, 2020: Thermal chains and entrainment in cumulus updrafts. Part I: Theoretical description. *J. Atmos. Sci.*, **77**, 3637–3660, https://doi.org/10.1175/JAS-D-19-0243.1.

Mulholland, J. P., J. M. Peters, and H. Morrison, 2021: How does vertical wind shear influence entrainment in squall lines? *J. Atmos. Sci.*, **78**, 1931–1946, https://doi.org/10.1175/JAS-D-20-0299.1.

Peters, J. M., and D. R. Chavas, 2021: Evaluating the conservation of energy variables in simulations of deep moist convection. *J. Atmos. Sci.*, **78**, 3229–3246, https://doi.org/10.1175/JAS-D-20-0351.1.

——, C. Nowotarski, and H. Morrison, 2019: The role of vertical wind shear in modulating maximum supercell updraft velocities. *J. Atmos. Sci.*, **76**, 3169–3189, https://doi.org/10.1175/JAS-D-19-0096.1.

——, H. Morrison, C. J. Nowotarski, J. P. Mulholland, and R. L. Thompson, 2020a: A formula for the maximum vertical velocity in supercell updrafts. *J. Atmos. Sci.*, **77**, 3747–3757, https://doi.org/10.1175/JAS-D-20-0103.1.

——, C. Nowotarski, and G. Mullendore, 2020b: Are supercells resistant to entrainment because of their rotation? *J. Atmos. Sci.*, **77**, 1475–1495, https://doi.org/10.1175/JAS-D-19-0316.1.

——, ——, and J. P. Mulholland, 2020c: The influences of effective inflow layer streamwise vorticity and storm-relative flow on supercell updraft properties. *J. Atmos. Sci.*, **77**, 3033–3057, https://doi.org/10.1175/JAS-D-19-0355.1.

——, H. Morrison, A. C. Varble, W. M. Hannah, and S. E. Giangrande, 2020d: Thermal chains and entrainment in cumulus updrafts. Part II: Analysis of idealized simulations. *J. Atmos. Sci.*, **77**, 3661–3681, https://doi.org/10.1175/JAS-D-19-0244.1.

——, ——, G. J. Zhang, and S. W. Powell, 2021: Improving the physical basis for updraft dynamics in deep convection parameterizations. *J. Adv. Model. Earth Syst.*, **13**, e2020MS002282, https://doi.org/10.1029/2020MS002282.

Prosser, N. E., and D. S. Foster, 1966: Upper air sounding analysis by use of an electronic computer. *J. Appl. Meteor. Climatol.*, **5**, 296–300, https://doi.org/10.1175/1520-0450(1966)005<0296:UASABU>2.0.CO;2.

Riehl, H., and J. S. Malkus, 1958: On the heat balance in the equatorial trough zone. *Geophysica*, **6**, 503–538.

Romps, D. M., 2008: The dry-entropy budget of a moist atmosphere. *J. Atmos. Sci.*, **65**, 3779–3799, https://doi.org/10.1175/2008JAS2679.1.

——, 2010: A direct measure of entrainment. *J. Atmos. Sci.*, **67**, 1908–1927, https://doi.org/10.1175/2010JAS3371.1.

——, 2015: MSE minus CAPE is the true conserved variable for an adiabatically lifted parcel. *J. Atmos. Sci.*, **72**, 3639–3646, https://doi.org/10.1175/JAS-D-15-0054.1.s

——, 2021: Accurate expressions for the dewpoint and frost point derived from the Rankine–Kirchhoff approximations. *J. Atmos. Sci.*, **78**, 2113–2116, https://doi.org/10.1175/JAS-D-20-0301.1.

——, and Z. Kuang, 2010: Do undiluted convective plumes exist in the upper troposphere? *J. Atmos. Sci.*, **67**, 468–484, https://doi.org/10.1175/2009JAS3184.1.

Simpson, J., and V. Wiggert, 1969: Models of precipitating cumulus towers. *Mon. Wea. Rev.*, **97**, 471–489, https://doi.org/10.1175/1520-0493(1969)097<0471:MOPCT>2.3.CO;2.

Squires, P., and J. S. Turner, 1962: An entraining jet model for cumulo-nimbus updrafts. *Tellus*, **14A**, 422–434, https://doi.org/10.1111/j.2153-3490.1962.tb01355.x.

Thompson, R. L., R. Edwards, J. A. Hart, K. L. Elmore, and P. Markowski, 2003: Close proximity soundings within supercell environments obtained from the Rapid Update Cycle. *Wea. Forecasting*, **18**, 1243–1261, https://doi.org/10.1175/1520-0434(2003)018<1243:CPSWSE>2.0.CO;2.

——, C. M. Mead, and R. Edwards, 2007: Effective storm-relative helicity and bulk shear in supercell thunderstorm environments. *Wea. Forecasting*, **22**, 102–115, https://doi.org/10.1175/WAF969.1.

Unidata, 2021: MetPy: A Python Package for Meteorological Data, version 1.1.0. UCAR/Unidata, accessed 1 May 2021, https://doi.org/10.5065/D6WW7G29.

Weisman, M. L., and J. B. Klemp, 1982: The dependence of numerically simulated convective storms on vertical wind shear and buoyancy. *Mon. Wea. Rev.*, **110**, 504–520, https://doi.org/10.1175/1520-0493(1982)110<0504:TDONSC>2.0.CO;2.

Xu, K., and K. Emanuel, 1989: Is the tropical atmosphere conditionally unstable? *Mon. Wea. Rev.*, **117**, 1471–1479, https://doi.org/10.1175/1520-0493(1989)117<1471:ITTACU>2.0.CO;2.

Zhang, G. J., 2009: Effects of entrainment on convective available potential energy and closure assumptions in convective parameterization. *J. Geophys. Res.*, **114**, D07109, https://doi.org/10.1029/2008JD010976.

Zipser, E. J., 2003: Some views on hot towers after 50 years of tropical field programs and two years of TRMM data. *Cloud Systems, Hurricanes, and the Tropical Rainfall Measuring Mission (TRMM): A Tribute to Dr. Joanne Simpson, Meteor. Monogr.*, No. 51, Amer. Meteor. Soc., 50–59.